Environmental Modulation of Mechanical and Thermodynamic Forcing from Cold Pool Collisions

NICHOLAS M. FALK[a] AND SUSAN C. VAN DEN HEEVER[a]

[a] *Department of Atmospheric Science, Colorado State University, Fort Collins, Colorado*

(Manuscript received 21 January 2022, in final form 23 September 2022)

ABSTRACT: Cold pools can initiate new convection by increasing vertical velocity (mechanical forcing) and locally enhancing moisture content (thermodynamic forcing). This study investigates the impact of the environment on mechanical and thermodynamic forcing from cold pool collisions. An ensemble of high-resolution numerical simulations was conducted that tested the sensitivity of cold pool collisions to three parameters: 1) the initial temperature deficit of cold pools, 2) the initial distance between cold pools, and 3) the static stability and moisture content of the environment. These parameters are tested in the absence of condensation, surface fluxes, radiation, and wind shear. Colder initial cold pools increase mechanical and thermodynamic forcing owing to greater horizontal winds during collisions. For all environments tested, mechanical forcing peaked robustly at an optimal initial distance between the cold pools due to a balance between the creation and dissipation of kinetic energy, and the different phases of density current evolution. Thermodynamic forcing peaked for greater initial cold pool distances than those associated with mechanical forcing. Decreased low-level static stability and an increased vertical gradient in low-level moisture enhanced mechanical and thermodynamic forcing, respectively. It is also shown that the initial temperature deficit had the greatest impact on mechanical and thermodynamic forcing, followed by the environment, and finally the initial separation distance. Finally, cold pool collisions are classified as "mechanically strong" or "mechanically weak," where mechanically strong collisions increased mechanical forcing beyond that driven by the initial outward spreading of the cold pools. An analogous classification of "thermodynamically strong/weak" is also presented.

KEYWORDS: Cold pools; Convective storms; Storm environments

1. Introduction

Convective cold pools have been observed across the globe in disparate environments from Florida and Ohio (e.g., Byers and Braham 1949), to Colorado, Wyoming, and Nebraska (e.g., van den Heever et al. 2021), to the Amazon (e.g., Lima and Wilson 2008), the Arabian Peninsula (e.g., Miller et al. 2008), and across the tropical oceans (e.g., Tompkins 2001; Feng et al. 2015; Reid et al. 2022, manuscript submitted to *Bull. Amer. Meteor. Soc.*). The environment in which a cold pool forms and propagates has a large impact on the properties of that cold pool (e.g., Liu and Moncrieff 2000), and thus the differences between these environments may lead to critical differences in important cold pools processes, such as the lofting and transport of aerosols like pollen and dust (e.g., Seigel and van den Heever 2012a), as well as the initiation of new convection by cold pool collisions (e.g., Droegemeier and Wilhelmson 1985b,a).

Delving into environmental impacts on cold pools first, the moisture content of an environment strongly modulates cold pool temperature deficits and moisture perturbations. Moist maritime conditions limit evaporation, and thus evaporative cooling, often leading to cold pools with temperature deficits of around 1 K (Tompkins 2001). In such environments, water vapor "rings" are often observed, with cold pools having diminished water vapor mixing ratios in their centers and enhanced water vapor mixing ratios at their edges (Tompkins 2001; Langhans and Romps 2015; Schlemmer and Hohenegger 2016; Torri and Kuang 2016). However, Chandra et al. (2018) found that water vapor rings were erroneously pronounced in numerical simulations when compared with observations. In contrast, drier continental conditions are conducive to more evaporative cooling, leading to cold pools with temperature deficits of up to 17 K (Engerer et al. 2008). Drager et al. (2020) demonstrated that in these environments the permanent wilting point–the soil moisture below which plants are unable to extract water from the soil–plays a key role in determining the moisture structure of cold pools. A water vapor ring structure may form when the soil is moister than the permanent wilting point, while a "puddle" of enhanced water vapor throughout cold pools may be present when the soil is drier than the permanent wilting point.

The strength and vertical profile of the environmental static stability is another environmental property that may greatly affect the propagation of cold pools. Liu and Moncrieff (2000) noted that there are three ways in which low-level static stability influences cold pools. First, there is a stabilization effect in which environmental stability leads to parcels that are lifted upward thereby becoming negatively buoyant. This negative buoyancy acts to oppose the cold pool lifting and becomes more forceful as static stability increases (Liu and Moncrieff 2000). The stability effect conversely opposes downdrafts associated with cold pools by making them positively buoyant. Second, there is an adiabatic cooling mechanism in which mechanically lifted ambient air affects the horizontal pressure gradient and can increase or decrease the propagation speed of cold pools. Finally, the radiation of energy by gravity waves

Corresponding author: Nicholas M. Falk, nick.falk@colostate.edu

DOI: 10.1175/JAS-D-22-0020.1

may slow down cold pools in continuously stratified environments as well as in environments with deep stable stratification above neutral stratification. Expanding on this research, Seigel and van den Heever (2012b) found that cold pools in environments with shallow stable stratification on top of neutral stratification do not slow down if the stable layer is shallow enough to avoid acting as a gravity wave ducting layer.

We now turn our attention to cold pool collisions. Observations have shown that collisions between cold pools are an important mechanism in the generation of new convective storms. Wilson and Schreiber (1986) noted that collisions between boundary layer convergence lines, often the edges of cold pools, enhanced an existing storm or initiated a new storm 84% of the time. In the southwest Amazon on a day with minimal synoptic forcing, 52% of storms were initiated from cold pools with 36% initiating from non-colliding cold pools and 16% from colliding cold pools (Lima and Wilson 2008). Analysis of three colliding cold pool case studies in Colorado also found that in each case the warmer cold pool was lifted to sufficient heights over the colder cold pool to initiate convection (Intrieri et al. 1990).

Numerical models have been used to expand the understanding of processes that occur during cold pool collisions. Droegemeier and Wilhelmson (1985b,a) investigated convection initiation from cold pool collisions and noted that the air was "literally squeezed out" of the space between the cold pools, thereby creating a pair of storms on either side of the line connecting the initial warm bubbles. Torri and Kuang (2019) also demonstrated that cold pools in tropical maritime regions tend to be clustered, often colliding within 10 min of forming, and that the collisions deform cold pools into noncircular shapes. They argue that collisions are a key dynamical process of cold pools. Meyer and Haerter (2020, hereinafter MH20) tested two-cold pool and three-cold pool collisions in dry, uniform environments without wind shear. They showed that two-cold pool collisions created larger vertical velocities than the collisions between three cold pools, but that three-cold pool collisions created more total updraft mass flux. They also noted that cold pools that start farther apart produce smaller peak vertical velocities later in the simulation and that collision-induced updrafts are shallower in statically stable environments when compared with statically neutral environments.

Cold pool collisions, along with individual cold pools, initiate convection through two mechanisms (Torri et al. 2015): mechanical forcing (Droegemeier and Wilhelmson 1985b,a) and thermodynamic forcing (Tompkins 2001). Mechanical forcing refers to the creation of new convection by the process of physically lifting environmental air up and over the cold pool edge, or gust front, so that it reaches the level of free convection (LFC) (Purdom 1976; Weaver and Nelson 1982; Droegemeier and Wilhelmson 1985b,a; Meyer and Haerter 2020). Thermodynamic forcing, on the other hand, refers to an increase in water vapor mixing ratio at cold pool edge that lowers the LFC and can, but does not always, decrease the convective inhibition (CIN) (Tompkins 2001; Feng et al. 2015; Langhans and Romps 2015). This may decrease the amount of lifting needed to initiate convection and reduce the negative effects of entrainment thereby enhancing the likelihood that convection will occur. In maritime environments, some studies argue that thermodynamic forcing is more important than mechanical forcing (e.g., Tompkins 2001) while others argue that both play a critical role (e.g., Torri et al. 2015). Considering continental environments, mechanical forcing is known to be important in many cases (e.g., Rotunno et al. 1988) but there has been little study on the thermodynamic forcing in continental environments.

Given the strong modulation of cold pool properties by the background environment, and the lack of prior research on the effects of this modulation on cold pools collisions, the goal of this study is to investigate the sensitivity of mechanical and thermodynamic forcing produced by cold pool collisions to various environmental characteristics. An idealized model is used to simulate a large number of cold pool collisions where the background environment, along with the initial temperature deficit of the cold pools and the initial distance between the cold pools, is varied. Section 2 describes the model setup and experimental design of these simulations. The dynamics and thermodynamics of a cold pool collision are examined in section 3. Section 4 discusses the effects of the tested parameters on cold pool collisions. Conclusions of this work are finally presented in section 5.

2. Methods

a. Model setup

Simulations were run using a high resolution nonhydrostatic two-dimensional model. The model is quasi compressible with an anelastic modification following Wilhelmson and Chen (1982). Such models have been found to be a useful tool for investigating cold pools (Liu and Moncrieff 1996, 2000; Seigel and van den Heever 2012b; Grant and van den Heever 2016). While three-dimensional models perform better in capturing some of the processes important for cold pools, such as the breakdown of Kelvin–Helmholtz waves (Grant and van den Heever 2016), the computational expediency of two-dimensional simulations allows for large numbers of simulations to be run at higher grid resolutions, and hence for a more thorough exploration of the associated parameter spaces.

The model utilized for this study solved the following equations:

$$\frac{\partial u}{\partial t} = -\frac{\partial uu}{\partial x} - \frac{1}{\overline{\rho}}\frac{\partial \overline{\rho} uw}{\partial z} - c_{p_d}\overline{\theta}_v\frac{\partial \pi'}{\partial x} + K_{mx}\frac{\partial^2 u}{\partial x^2} + K_{mz}\frac{\partial^2 u}{\partial z^2}, \tag{1}$$

$$\frac{\partial w}{\partial t} = -\frac{\partial uw}{\partial x} - \frac{1}{\overline{\rho}}\frac{\partial \overline{\rho} ww}{\partial z} - c_{p_d}\overline{\theta}_v\frac{\partial \pi'}{\partial z} + g\left(\frac{\theta'}{\overline{\theta}} + 0.61r'_v\right) + K_{mx}\frac{\partial^2 w}{\partial x^2} + K_{mz}\frac{\partial^2 w}{\partial z^2}, \tag{2}$$

$$\frac{\partial \theta'}{\partial t} = -\frac{\partial u\theta'}{\partial x} - \frac{1}{\overline{\rho}}\frac{\partial \overline{\rho} w\theta'}{\partial z} - w\frac{d\overline{\theta}}{dz} + K_{hx}\frac{\partial^2 \theta'}{\partial x^2} + K_{hz}\frac{\partial^2 \theta'}{\partial z^2}, \tag{3}$$

$$\frac{\partial \pi'}{\partial t} = -\frac{\overline{c}_s^2}{\overline{\rho} c_{p_d} \overline{\theta}_v^2}\left(\overline{\rho}\overline{\theta}_v \frac{\partial u}{\partial x} + \frac{\partial \overline{\rho}\overline{\theta}_v w}{\partial z}\right) + K_{hx}\frac{\partial^2 \pi'}{\partial x^2} + K_{hz}\frac{\partial^2 \pi'}{\partial z^2}, \quad \text{and} \tag{4}$$

$$\frac{\partial r_v'}{\partial t} = -\frac{\partial u r_v'}{\partial x} - \frac{1}{\overline{\rho}}\frac{\partial \overline{\rho} w r_v'}{\partial z} - w\frac{d\overline{r_v}}{dz} + K_{hx}\frac{\partial^2 r_v'}{\partial x^2} + K_{hz}\frac{\partial^2 r_v'}{\partial z^2}, \tag{5}$$

using the leapfrog scheme in time and centered differencing in space. Overbars represent environmental values, and primes represent perturbations from these environmental values; u (m s^{-1}) is the horizontal component of the wind velocity vector, w (m s^{-1}) is the vertical component of the wind velocity vector, θ (K) is the potential temperature, r_v (kg kg^{-1}) is the water vapor mixing ratio, C_{p_d} (J kg^{-1} K^{-1}) is the specific heat capacity of dry air, g (m s^{-2}) is the acceleration due to gravity, $\overline{c}_s$ (m s^{-1}) is the speed of sound, K_{mx} and K_{mz} (m^2 s^{-1}) are the eddy diffusion coefficients for winds, and K_{hx} and K_{hx} (m^2 s^{-1}) are the eddy diffusion coefficients for scalars. Given pressure p (hPa), reference pressure p_0 = 1000 hPa, and dry air gas constant R_d (J kg^{-1} K^{-1}), the Exner function π is written as

$$\pi = (p/p_0)^{R_d/C_{Pd}}. \tag{6}$$

The 2D Arakawa C grid used was 803 points by 160 points in the horizontal (x) and vertical (z) directions, respectively. Sensitivity tests using a grid 3 times the size in the horizontal (2409 points), yielded maximum vertical velocities and water vapor mixing ratios that differed by less than 1.4% from the grid with 803 points. Grid spacings of 100 m in the horizontal and 50 m in the vertical were chosen as such spacings have been shown to be necessary to accurately represent cold pool processes (Grant and van den Heever 2016). The constant eddy diffusion coefficient values used were K_{mx} = 50 m^2 s^{-1}, K_{mz} = 25 m^2 s^{-1}, K_{hx} = 150 m^2 s^{-1}, and K_{hz} = 75 m^2 s^{-1}, which are the same as those used by Grant and van den Heever (2016) for the aforementioned grid spacings. The time step was 0.25 s. A Robert–Asselin filter was applied using gamma of 0.2. A Rayleigh damping layer was implemented in the uppermost 300 m of the model domain with a time scale of 60 s to avoid reflection of gravity waves off the model top.

Periodic lateral boundaries were applied. The lower freeslip boundary was implemented as follows. The lowest scalar height level was below the ground at z = −25 m. The next vertical level was above the ground at z = 25 m. All values at this bottommost level (z = −25 m) were set to be identical to the level above (z = 25 m) to ensure that all gradients across the lower boundary were zero. The lowest level on the staggered grid for vertical velocity was at z = 0 m and w = 0 m s^{-1} was imposed as a lower boundary condition.

To simplify the analysis of environmental factors on cold pool collisions, neither surface fluxes nor radiation were utilized, and there was no base state wind. Full-model output was saved every minute, while domainwide values of maximum horizontal (absolute value) and vertical velocity, and minimum potential temperature were saved every time step. All of the model settings used to conduct these experiments are summarized in Table 1. The cold pools were initiated using cosine smoothed bubbles centered at the surface with vertical radii of 1000 m and horizontal radii of 2500 m. Two cold pools were initiated at a specified distance apart in each simulation and allowed to subsequently collide.

TABLE 1. Summary of settings used in the 2D anelastic model to conduct the experiments.

Model setting	Value/type
Model type	2D anelastic, nonhydrostatic
Time step	0.25 s
Horizontal grid spacing	100 m
Vertical grid spacing	50 m
No. of x points	803
No. of z points	160
Simulation duration	1 h
Data output frequency	1 min
Speed of sound (for anelastic approximation)	50 m s^{-1}
Lateral boundary conditions	Cyclic
Surface boundary condition	Free slip
Rayleigh damping layer depth	300 m
Rayleigh damping layer time scale	60 s
Initial bubble x radius	2500 m
Initial bubble z radius	1000 m
Initial bubble temperature deficit	Varies from 1 to 20 K every 1 K
Initial distance between bubbles	Varies from 0 to 27 200 m every 800 m

While water vapor was allowed to freely advect, diffuse, and influence buoyancy, water vapor was not allowed to condense, and no other microphysical processes were accounted for. Including condensation would allow for convection initiation to be directly studied; however, preventing condensation and the subsequent cloud processes facilitates the analysis of a large number of simulations. Disentangling the effects of subsequent moist convection and the production of new potential cold pools from the effects of the initial cold pools on such a large set of simulations would be impractical. Thus, analysis focuses on the domain and time maximum values of vertical velocity and water vapor mixing ratio perturbation, while the depths and durations of these variables are also discussed.

b. Experimental design

Eight suites of sensitivity experiments were conducted (Table 2). Each suite included simulations in which the initial minimum potential temperature perturbation (hereinafter initial temperature deficit) of the cold pools was varied from 1 to 20 K at intervals of 1 K (20 values), and the initial edge-to-edge distance (hereinafter initial distance) of the cold pools was varied from 0 to 27 200 m at intervals of 800 m (35 values). All combinations of these two parameters were tested for a total of 700 simulations per environment experiment suite and thus 5600 simulations in total. While the temperature

TABLE 2. The nomenclature and descriptions for each of the 16 sensitivity experiment suites. For each suite, 700 simulations were run in which the initial temperature deficit of the cold pools was varied from 1 to 20 K at an interval of 1 K and the initial edge-to-edge distance between the cold pools was varied from 0 to 27 200 m at an interval of 800 m. Suites are grouped by dry and moist environments.

Expt suite group	Expt suite long name	Expt suite abbreviation	Expt suite description
DRY	Dry isentropic	DI	A profile with constant potential temperature of 300 K and no moisture
DRY	Half-stability nocturnal	NT_HS	A profile with a surface-to-1-km-deep stable layer with Brunt–Väisälä frequency of 0.005 s^{-1} that is isentropic above 1 km with no moisture, representative of a nocturnal atmosphere over land
DRY	Standard-stability nocturnal	NT	The NT_HS experiment, but with the stable layer having a Brunt–Väisälä frequency of 0.01 s^{-1}
DRY	Double-stability nocturnal	NT_DS	The NT_HS experiment, but with the stable layer having a Brunt–Väisälä frequency of 0.02 s^{-1}
MOIST	Weisman–Klemp	WK	A profile similar to that used by Weisman and Klemp (1982), which is representative of the midwestern United States in spring
MOIST	CAMP^{2}Ex SF12 S10 environment	S10	The profile taken during CAMP^{2}Ex science flight 12 by dropsonde 10; this profile was taken over tropical ocean surrounding the Philippines just ahead of an outflow boundary
MOIST	Sokolowsky environment	SK	The midstability environment used by Sokolowsky et al. (2020), representative of the tropical ocean surrounding the Philippines
MOIST	CAMP^{2}Ex SF07 S07 environment	S07	The profile taken during CAMP^{2}Ex science flight 7 by dropsonde 7; this profile was taken over tropical ocean surrounding the Philippines just ahead of an advancing cold pool

perturbations in cold pools are negative, temperature *deficits* inside cold pools are positive and will often be referred to in this text for clarity. The range of initial temperature deficits was chosen based on the range of observed cold pool temperature deficits: from 1 K or less in maritime environments (Tompkins 2001) up to 17 K in continental environments (Engerer et al. 2008). MH20 tested initial distances of 10, 12, and 15 km. The current study extended the distances investigated, testing the closest initial distance possible (0 m), for the sake of completeness, up to almost 2 times HM20's tested maximum (27 200 m). Beyond this distance, collisions between the cold pools in the first environment tested did not produce vertical velocities greater than those produced by the preliminary spreading of the cold pools. The sensitivity experiment suites differ only in their base-state environments.

While MH20 tested two different dry idealized environments, Fig. 1 shows skew T–log$p$ diagrams of the eight different idealized, maritime, and continental environments tested here. The experiment suites are divided into two different groups, a dry group of four idealized environments with no moisture and in which the low-level static stability is increased, and a moist group of four environments in which the low-level moisture increases along with other environmental variations and that includes both theoretical and observed environments. These two experiment-suite groups are referred to as the DRY and MOIST groups, respectively, throughout the paper.

In increasing order of low-level static stability, the DRY group begins with the dry isentropic environment (DI), which had no water vapor and a constant potential temperature of 300 K throughout. This option was selected to assess an environment without static stability and compare it with statically stable environments. Additionally, dry isentropic environments are commonly used in idealized cold pool modeling studies (Liu and Moncrieff 2000; Seigel and van den Heever 2012b; MH20). The half-stability nocturnal environment (NT_HS) also had no water vapor and consisted of a layer from 0 to 1 km AGL with a constant Brunt–Väisälä frequency of 0.005 s^{-1} and was dry isentropic above 1 km AGL. NT_HS is representative of stable nocturnal boundary layers. The nocturnal (NT) and double stability nocturnal (NT_DS) environments were identical to NT_HS except for having Brunt–Väisälä frequencies of 0.01 and 0.02 s^{-1}, respectively, for the 0–1 km layer. Thus, DI, NT_HS, NT, and NT_DS provide a set of experiment suites where the low-level static stability was steadily increased from 0 to 0.02 s^{-1}, similar to Liu and Moncrieff (2000).

In increasing order of low-level moisture, the first experiment in the MOIST group is the Weisman–Klemp environment (WK) suite. The temperature profile is the same as that used by Weisman and Klemp (1982), and is representative of atmospheric conditions in the midwestern United States in spring. The dewpoint profile used here is greater just above the surface but generally lower at the top of the boundary layer and aloft relative to the dewpoint profile used by Weisman and Klemp (1982). The S10 environment has the second lowest low-level moisture of suites in the MOIST group. This environment was taken from a dropsonde released during the CAMP^{2}Ex field campaign (Reid et al. 2021, manuscript submitted to *Bull. Amer. Meteor. Soc.*). This sonde was dropped just outside a cold pool over the tropical ocean around the Philippines. Because the S10 sonde was dropped from an

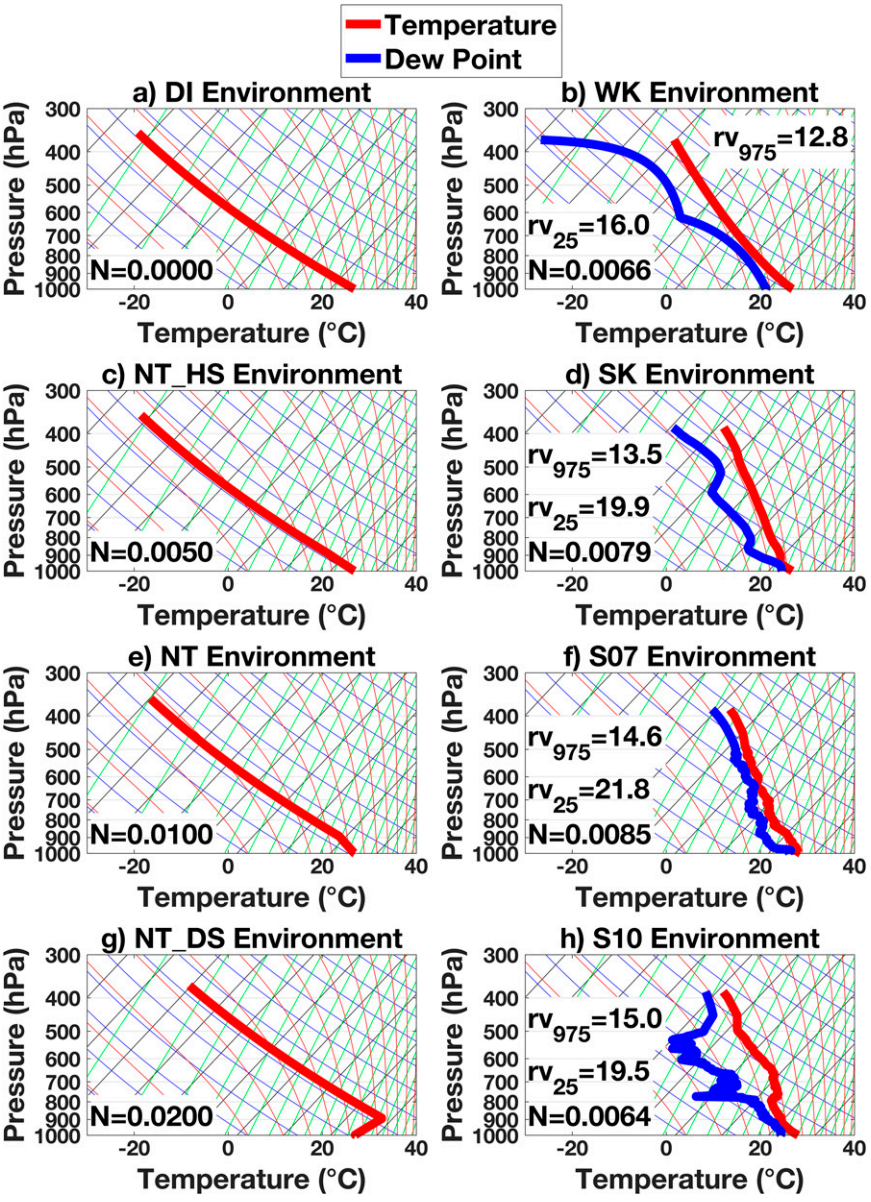

FIG. 1. Skew T–log$p$ diagrams for all of the different environments tested. No base state wind was used in any experiment. Each panel lists the water vapor mixing ratio (g kg^{-1}) at 975 (rv_{975}) and 25 m (rv_{25}) for those experiments with moisture. The Brunt–Väisälä frequency of the 25–975 m layer N (s^{-1}) is listed for all environments.

altitude lower than the top of the model domain, ERA5 reanalysis was used above 6 km AGL to the model top. Linear smoothing with height between ERA5 and the dropsonde data was applied between 5 and 6 km in the S10 environment to ensure a continuous atmospheric profile. The midstability environment used by Sokolowsky et al. (2022) was used to represent tropical maritime conditions, and has the second highest low-level moisture of experiments in the MOIST group. The S07 environment has the most low-level moisture of experiments in the MOIST group. S07 is from another CAMP^{2}Ex dropsonde dropped just ahead of a cold pool. This environment incorporates ERA5 data in the same way the S10 environment does. Note that while the SK, S07, and S10 environments are all representative of maritime conditions, SK was from an idealized numerical experiment, while S07 and S10 used observational data. Since the environments in the MOIST group include observations (S07 and S10), there are additional differences between them (e.g., low-level static stability), beyond the variation in low-level moisture. The S07 and S10 environments were selected because in both of these cases dropsondes were dropped in close succession, both within and just outside cold pools. Such observations of cold pools are

uncommon. Thus, these cases were chosen because they provided an excellent opportunity to examine maritime cold pools.

The set of environments tested here therefore includes idealized environments in which cold pools are often examined (DI) or are representative of real conditions that cold pools encounter (NT_HS, NT, and NT_DS), including a continental (WK), and maritime environments (SK, S07, S10) conducive to convection. Thus, the examined collisions occurred within a range of different environments representative of many conditions supporting cold pool development.

3. Dynamic and thermodynamic cold pool collision processes

The general nomenclature for each sensitivity experiment follows the format: experiment_abbrevation_Txx_Dyyy where experiment_abbrevation is the abbreviated name of each experiment suite (Table 2), xx is the initial temperature deficit of the simulated cold pools in kelvins, and yyy is the initial distance between cold pools in hectometers (for the sake of simplicity). In this section the WK_T10_D136 (Weisman–Klemp environment, 10-K initial temperature deficit, and 13 600 m initial distance) simulation is analyzed in detail to describe the physical processes that occur before, during, and after a typical cold pool collision. This simulation is singled out because its initial temperature deficit of 10 K and its initial distance of 13 600 m between cold pools are close to the median values tested. The WK experiment suite was chosen because the WK environment has a low-level Brunt–Väisälä frequency of 0.0066 s^{-1}, which is also close to the median value of 0.007 25 s^{-1}.

Vertical velocity and water vapor mixing ratio form the focus of the subsequent analysis. The advection of vertical velocity (ADV_W), the buoyancy (BUOY_W), the vertical perturbation pressure gradient force (PRESS_W), and the diffusion of vertical velocity (DIFF_W) are respectively defined as

$$\text{ADV\_W} = -\frac{\partial uw}{\partial x} - \frac{1}{\overline{\rho}}\frac{\partial \overline{\rho} ww}{\partial z}, \tag{7}$$

$$\text{BUOY\_W} = g\left(\frac{\theta'}{\overline{\theta}} + 0.61r_v'\right), \tag{8}$$

$$\text{PRESS\_W} = -c_{p_d}\overline{\theta_v}\frac{\partial \pi'}{\partial z}, \quad \text{and} \tag{9}$$

$$\text{DIFF\_W} = K_{mx}\frac{\partial^2 w}{\partial x^2} + K_{mz}\frac{\partial^2 w}{\partial z^2}. \tag{10}$$

Using these abbreviations, Eq. (2) can be rewritten as

$$\partial w/\partial t = \text{ADV\_W} + \text{PRESS\_W} + \text{BUOY\_W} + \text{DIFF\_W}. \tag{11}$$

While BUOY_W and PRESS_W represent different processes, these terms are often large and in opposition to each other. When BUOY_W and PRESS_W are in balance, and the other terms of Eq. (2) are equal to zero, the atmosphere is in hydrostatic balance. Thus, examining the sum of BUOY_W and PRESS_W (BUOY_W + PRESS_W) makes the overall thermodynamic effect on vertical velocity clearer than examining these terms individually. BUOY_W + PRESS_W can equivalently be thought of as the total nonadvective vertical acceleration.

The horizontal advection of the water vapor mixing ratio perturbation (ADV_H_rvp), vertical advection of water vapor mixing ratio perturbation (ADV_V_rvp), and diffusion of water vapor mixing ratio perturbation (DIFF_rvp) are respectively defined as

$$\text{ADV\_H\_rvp} = -\frac{\partial ur_v'}{\partial x}, \tag{12}$$

$$\text{ADV\_V\_rvp} = -\frac{1}{\overline{\rho}}\frac{\partial \overline{\rho} wr_v'}{\partial z} - w\frac{d\overline{r_v}}{dz}, \quad \text{and} \tag{13}$$

$$\text{DIFF\_rvp} = K_{hx}\frac{\partial^2 r_v'}{\partial x^2} + K_{hz}\frac{\partial^2 r_v'}{\partial z^2}. \tag{14}$$

Thus, Eq. (5) can be rewritten as

$$\partial r_v'/\partial t = \text{ADV\_H\_rvp} + \text{ADV\_V\_rvp} + \text{DIFF\_rvp}. \tag{15}$$

At initialization, $w = 0$ and $r_v' = 0$ throughout the domain; thus Eq. (2) can be simplified to

$$\frac{\partial w}{\partial t} = -c_{p_d}\overline{\theta_v}\frac{\partial \pi'}{\partial z} + g\left(\frac{\theta'}{\overline{\theta}} + 0.61r_v'\right) = \text{PRESS\_W} + \text{BUOY\_W}. \tag{16}$$

Similarly, Eq. (5) can be simplified as

$$\frac{\partial r_v'}{\partial t} = -w\frac{d\overline{r_v}}{dz} = \text{ADV\_V\_rvp}. \tag{17}$$

Thus, the only processes that can produce vertical velocity from an initial absence of vertical velocity are buoyancy and a vertical perturbation pressure gradient, and the only process that can initially produce water vapor perturbations is vertical advection, specifically vertical advection of base state water vapor. The remaining terms in Eqs. (11) and (15) cannot be said to explicitly produce vertical velocity or water vapor perturbations, but rather simply move them around.

a. *Processes before a cold pool collision*

After 1 min of simulation, the cold pool on the left side of the domain has changed little in shape from the initial temperature perturbation in the model (Fig. 2a). At this time, subsident motion is present in the center of the cold pool leading to divergent flow at the surface. The cold pool is colder than the base state environment and hence is negatively buoyant; however, the negative temperature perturbation of the cold pool also leads to a positive pressure perturbation inside of the cold pool (Fig. 3a). This positive pressure perturbation near the surface leads to PRESS_W > 0 (not shown). Thus, near the center of the cold pool, as |BUOY_W| > |PRESS_W|, subsident motion occurs because of the air being negatively buoyant. Conversely, near the edge of the cold pool, as |PRESS_W| > |BUOY_W|, air is accelerated upward owing to a positive vertical perturbation pressure

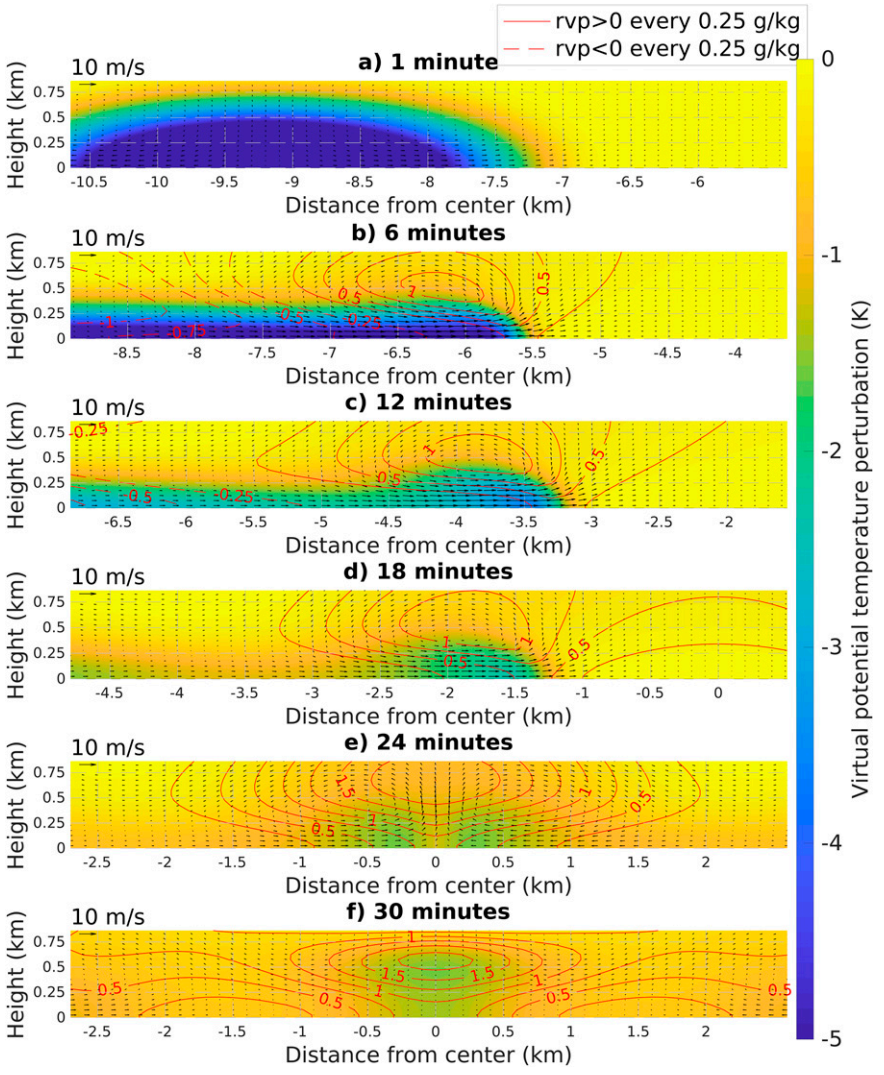

FIG. 2. The evolution of colliding cold pools over the first 30 min of the simulation, showing virtual potential temperature perturbation (shaded), water vapor mixing ratio perturbation (red contours every 0.25 g kg^{-1}), and winds for the WK_T10_D136 simulation at (a) 1, (b) 6, (c) 12, (d) 18, (e) 24, and (f) 30 min. Note that the portion of the domain shown is focused on the cold pool on the left side of the domain and that it moves in time as the cold pool propagates. The symmetric initialization of the model domain means that the cold pool on the right side of the domain is a mirror image of the left cold pool. The right cold pool does become evident in (e). This figure is plotted so that the aspect ratio of the cold pool is generally preserved.

gradient force (Fig. 3a). A small decrease in water vapor mixing ratio also exists in the center of the cold pool as a result of the subsident motion inside of the cold pool that advects dry air from above downward into the cold pool leading to ADV_V_rvp < 0 (Fig. 4a).

After 6 min the cold pool has rapidly flattened to a maximum height of ~500 m and spread ~1.5 km toward the center of the domain (Fig. 2b). As this cold pool advances toward the center of the domain, typical cold pool behavior is evident, with rising motion at the cold pool head, and subsident motion behind it (Goff 1976) (Figs. 2b–d). As at 1 min, rising motion is driven by a positive vertical perturbation pressure gradient force in front of the cold pool head and subsident motion behind the cold pool head by negative buoyancy in this region (Figs. 3b–d). Virtual potential temperature increases within the cold pool from 6 to 18 min, thereby reducing the perturbation from the environment and weakening the cold pool (Figs. 2b–d). As there is no source of diabatic heating or cooling following the initialization of the simulations, this progressive dissipation is due to the entrainment of environmental air into the cold pool. This entrainment weakens the lifting at the cold pool edge and the subsidence behind the cold pool head as both the buoyant force and vertical perturbation pressure gradient force are reduced in magnitude,

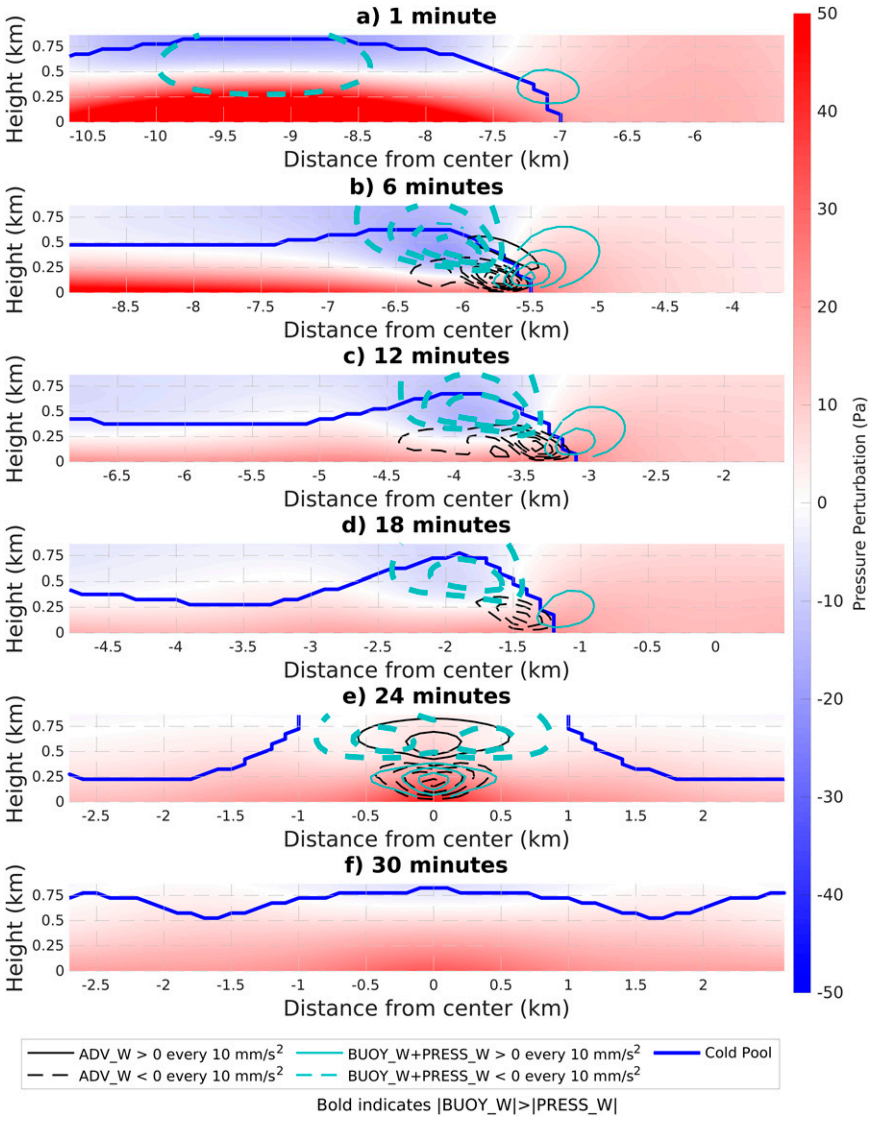

FIG. 3. Dynamics of two colliding cold pools over the first 30 min of the simulation: as in Fig. 2, but showing perturbation pressure (shaded), advection of vertical velocity [ADV_W; see Eq. (7)] (black contours), the sum of the buoyancy term and vertical perturbation pressure gradient term [BUOY_W + PRESS_W; see Eqs. (8) and (9)] (cyan contours), and the cold pool boundary (dark blue line) for the WK_T10_D136 simulation at (a) 1, (b) 6, (c) 12, (d) 18, (e) 24, and (f) 30 min. Thick cyan contours indicate that the magnitude of BUOY_W is greater than that of PRESS_W. Thin cyan contours indicate that the magnitude of PRESS_W is greater than that of BUOY_W. All contours are every 10 mm s^{-2}. Diffusion of vertical velocity (DIFF_W) is not plotted because it is much weaker than ADV_W and BUOY_W + PRESS_W. Note that the portion of the domain shown in each panel changes to keep the edge of the cold pool on the left side of the domain in view as it propagates.

leading to BUOY_W + PRESS_W being reduced in magnitude (Figs. 3b–d). The rising (sinking) motion and associated vertical advection of water vapor at the cold pool edge (center) (Figs. 4b–d) results in moistening (drying) at the cold pool edge (center) up through 18 min (Figs. 2c,d), resulting in a 2D water vapor-ring structure. The generation of a water vapor ring in this simulation is likely due in part to the lack of surface fluxes and/or evaporation to increase water vapor content. These results suggest that convergence can generate water vapor rings in the absence of other factors (e.g., surface fluxes).

b. *Processes during a cold pool collision*

The two cold pools collide at the center of the domain at 24 min (Fig. 2e); this is also the time period in which the largest domain maximum vertical velocity is observed. The pressure is locally enhanced at the surface at the location of the

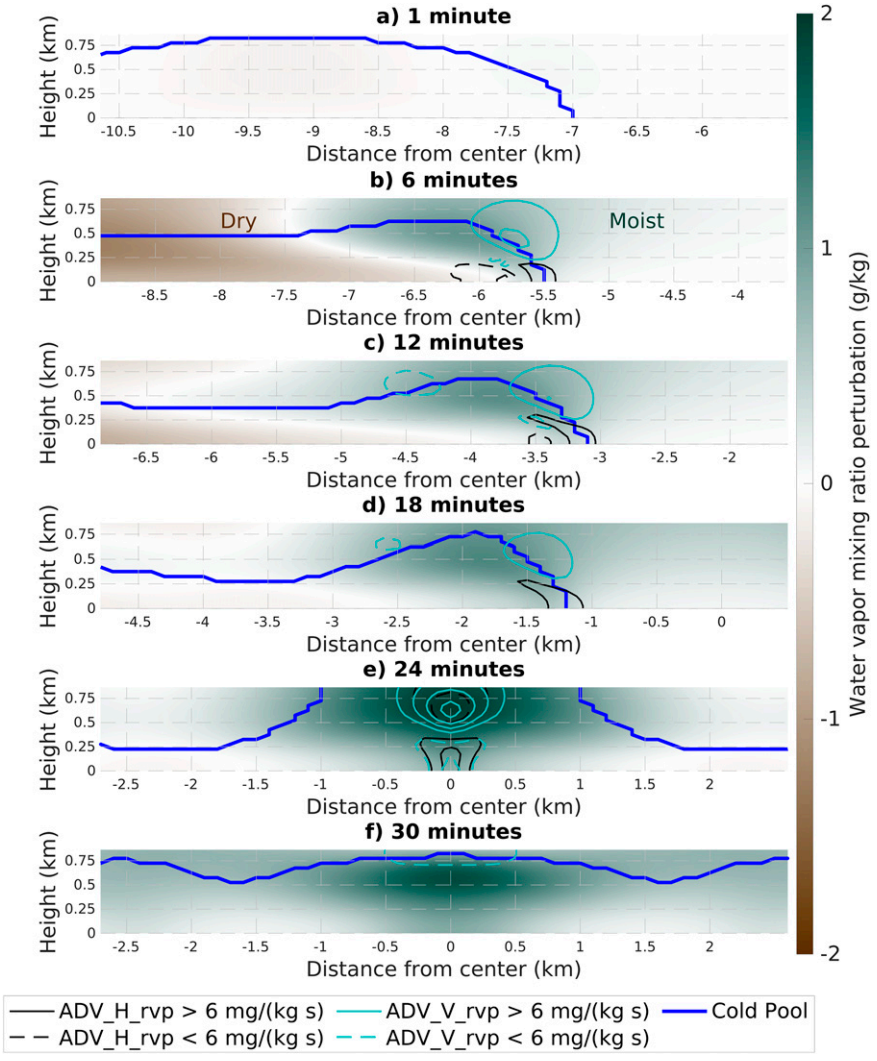

FIG. 4. Moisture transport associated with colliding cold pools over the first 30 min of the simulation: as in Fig. 2, but showing water vapor mixing ratio perturbation (shaded), horizontal advection of water vapor mixing ratio perturbation [(ADV_H_rvp; see Eq. (12)] (black contours), vertical advection of water vapor mixing ratio perturbation [(ADV_V_rvp; see Eq. (13)] (cyan contours), and the cold pool boundary (dark blue line) for the WK_T10_D136 simulation at (a) 1, (b) 6, (c) 12, (d) 18, (e) 24, and (f) 30 min. All contours are every 6 mg kg^{-1} s^{-1}. Diffusion of water vapor mixing ratio perturbation (DIFF_rvp) is not plotted because it is much weaker than ADV_H_rvp and ADV_V_rvp. Note that the portion of the domain shown in each panel changes to keep the edge of the cold pool on the left side of the domain in view as it propagates.

collision (Fig. 3e), as a result of the large horizontal convergence associated with the collision [Eq. (4)]. This produces a large, positive PRESS_W + BUOY_W below ~400 m at the location of the collision, thereby accelerating air upward. Collocated with this positive PRESS_W + BUOY_W are negative values of vertical velocity advection. Above ~400 m, the signs of these two trends reverse, with PRESS_W + BUOY_W < 0 and ADV_W > 0 (Fig. 3e). This change in sign in the vertical velocity advection is indicative that the vertical velocity produced below 400 m is being transported to above 400 m. Above 400 m, PRESS_W + BUOY_W < 0 as the air lofted during the collision is negatively buoyant as a result of two processes. First, some of the air lofted by the collision originates within the cold pools and hence is negatively buoyant. Second, the WK environment is stably stratified and thus, as air rises, its perturbation potential temperature decreases.

The collision-induced increase in vertical velocity increases the water vapor mixing ratio (Fig. 4e) and occurs in a similar manner to the vertical velocity. Below 400 m, large horizontal advection increases the water vapor content at the location of the collision, while vertical advection lifts it (Fig. 4e). Above

400 m, vertical advection increases moistening at the location of the collision while the horizontally divergent flow decreases the water vapor content.

c. *Processes after a cold pool collision*

As time progresses after the collision, the aforementioned negative buoyancy at the location of the collision deaccelerates the updraft. Six minutes after the collision, at the location of the collision, the air is weakly subsident due to this negative buoyancy, while the water vapor mixing ratio remains enhanced (Fig. 2f). This negative buoyancy, however, is nearly balanced by a positive vertical perturbation pressure gradient force leading to minimal positive or negative acceleration, as the atmosphere is nearly in hydrostatic balance (Fig. 3f). The weakly subsident motion decreases the water vapor mixing ratio at 30 min, but at rates much slower than the moistening during the collision (Fig. 4f).

4. Exploring the parameter space of cold pool collisions

In this section, the effects of the initial cold pool temperature deficit, initial distance between cold pools, and the thermodynamic environment on cold pool collisions are now addressed. The relative importance of each parameter is then assessed. The focus of this analysis is on the domain and time maximum vertical velocity (hereinafter W_max) and water vapor mixing ratio perturbation (hereinafter rvp_max) from the simulations. W_max is used as a proxy for mechanical forcing and rvp_max is used as a proxy for thermodynamic forcing. Recall that water vapor is not allowed to condense in these simulations, thereby preventing moist convection. CIN is not analyzed directly, as the focus of this work is on analyzing mechanical and thermodynamic forcing; however, it is worth noting that thermodynamic forcing can, but does not always, lower the CIN. Throughout this analysis, it is also often helpful to think in terms of kinetic and potential energy. An initially motionless cold pool has no kinetic energy but achieves a maximum in gravitational potential energy as a result of the presence of dense fluid above the surface. As the cold pool spreads out horizontally, the potential energy is converted to kinetic energy.

a. *The effect of the initial temperature deficit*

The WK experiment suite demonstrates that as the initial temperature deficit of cold pools increases, collisions between these cold pools generate monotonically increasing W_max and rvp_max (Fig. 5). This is also true in the mean for all of the other environments considered (Figs. 6a,c). The depths and durations of the vertical velocity and moisture perturbations produced by cold pool collisions also increase as the initial cold pools become colder (Figs. 7a,c,e,g) (widths of updrafts and moisture perturbations are not shown in Fig. 7 as the trends in widths are nearly identical to the trends in depths). Note that in Figs. 6 and 7, the experiments in the DRY group are in order of increasing low-level static stability (from DI to NT_HS) and the experiments in the MOIST group are in order of increasing low-level moisture (from WK to S07). Since cold pools tend to have greater temperature

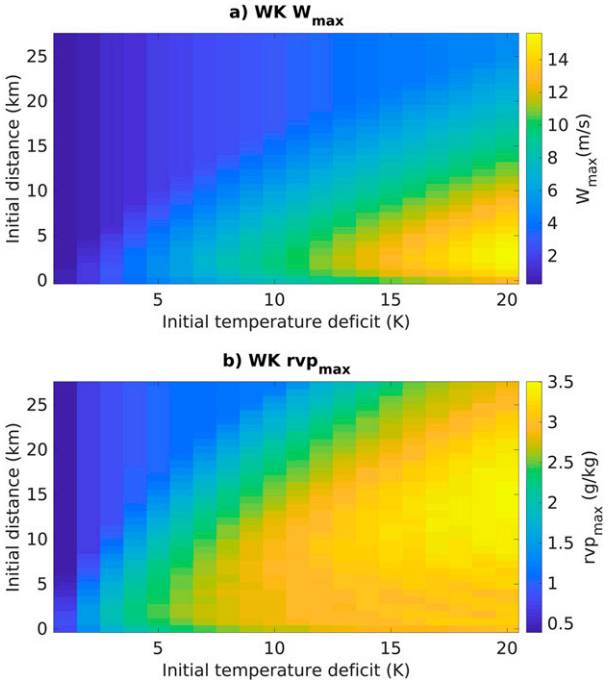

FIG. 5. Change in the proxies of mechanical and thermodynamic forcing from cold pool collisions with initial temperature deficit and initial distance: (a) W_max and (b) rvp_max from all simulations in the WK experiment suite. Note that the "0" initial distance row indicates simulations in which the initial cold pools start with their edges touching.

deficits in drier continental environments than in moister maritime environments, this indicates cold pool collisions should produce greater mechanical and thermodynamic forcing in continental environments relative to maritime environments. Hence, this suggests cold pool collisions in continental environments may initiate convection more frequently than those in maritime environments.

A cold pool with a larger initial temperature deficit will remain colder than a cold pool with a smaller initial temperature deficit (Fig. 8a). Thus, a pair of initially colder, stronger cold pools will be colder when they collide than will a pair of initially warmer, weaker cold pools. Colder cold pools also have greater horizontal winds at their outflow boundaries (Fig. 8b). This relationship arises from the fact that colder cold pools have more potential energy to convert to kinetic energy; they will therefore produce greater horizontal convergence, thereby leading to a greater near-surface pressure perturbation at the point of the collision, which in turn drives stronger updrafts. The stronger updrafts enhance the vertical advection of water vapor, thereby moistening the atmosphere during the collision.

Some of the sensitivity experiment suites were rerun with halved or doubled eddy diffusion coefficients to assess the impact of cold pool dissipation rates relative to initial cold pool temperature deficits (not shown). Cold pools that dissipated slower (faster) before they collided produced increased (decreased) W_max and rvp_max due to being relatively colder (warmer) when colliding, akin to cold pools with greater

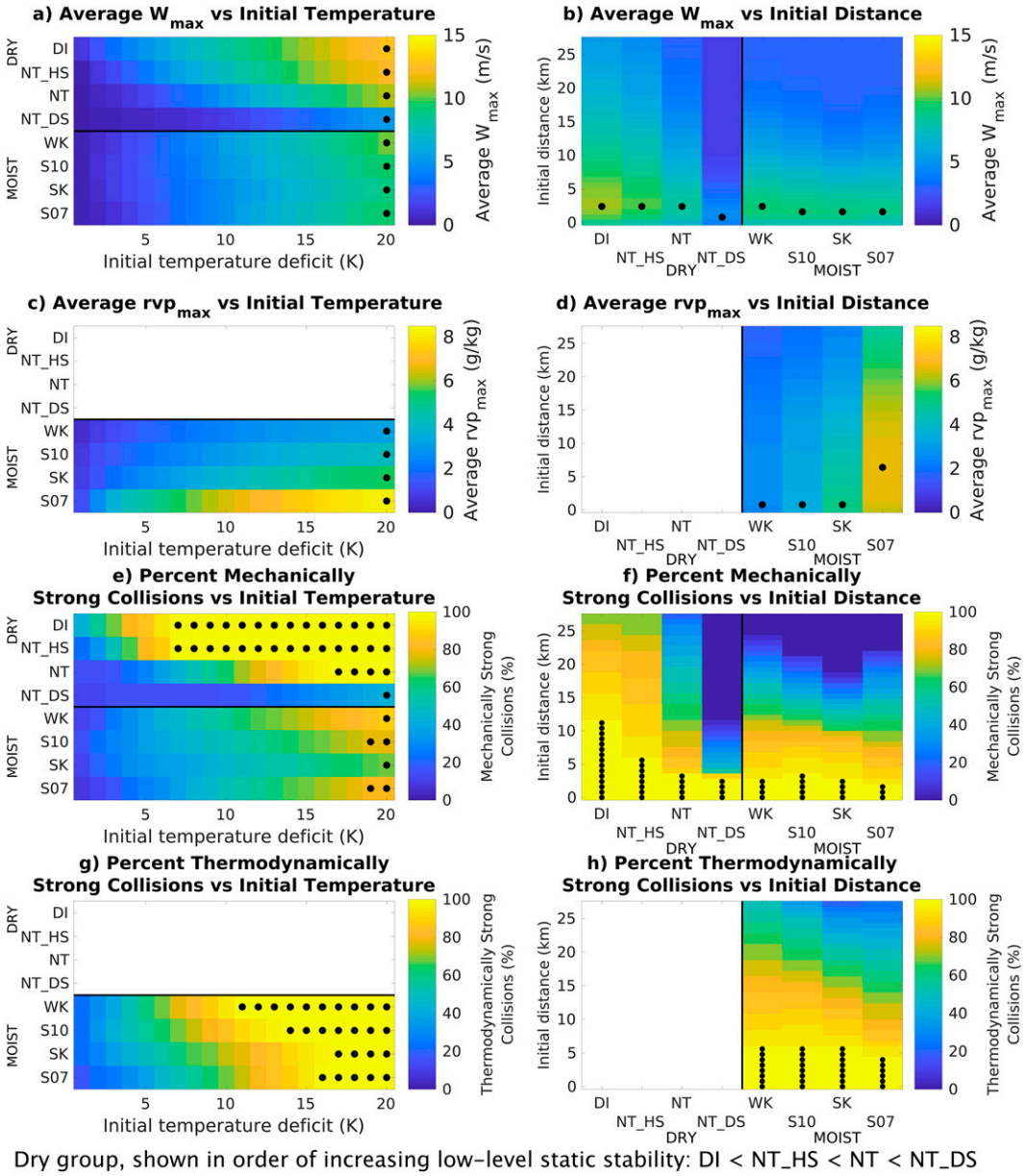

FIG. 6. Summary of mechanical forcing and thermodynamic forcing from all the experiment suites: the (a),(b) W_max; (c),(d) rvp_max; (e),(f) percent of collisions that are mechanically strong (see section 4b for this definition); and (g),(h) percent of collisions that are thermodynamically strong (see section 4b for this definition) for (left) all experiments averaged over all initial distances and (right) all initial temperature deficits. Because there is no moisture present in the DRY group of simulations, the respective areas for these experimental suites are left blank in (c), (d), (g), and (h). Black dots are placed for the maximum values in each experiment suite, with multiple dots if there are duplicates of the maximum value.

(smaller) initial temperature deficits. This suggests that the initial temperature deficits of the cold pools do not directly influence the mechanical and thermodynamic forcing produced by the collision. Rather, the temperature deficits of the cold pools when they are colliding is key. The initial temperature deficits of the cold pools play a large role in determining the temperature deficits of the cold pools during collision, and thus indirectly impact the mechanical and thermodynamic forcing produced.

b. *The effect of the initial distance between cold pools*

The relationship between the initial cold pool distance and W_max in the WK experiment suite is non-monotonic (Fig. 5a).

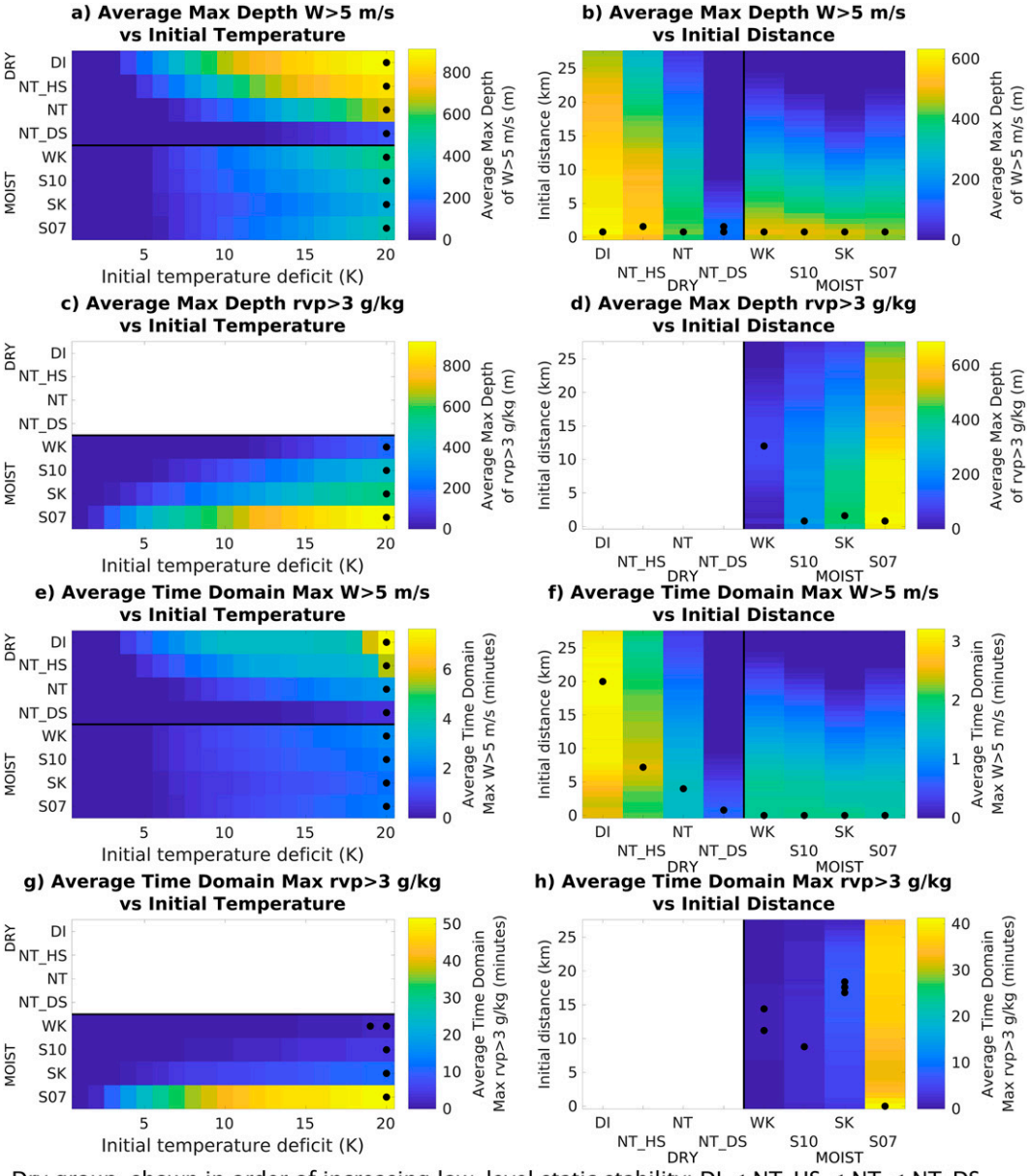

FIG. 7. Summary of depth and duration of vertical velocity and moisture enhancements from cold pool collisions, showing the (a),(b) maximum depth of 5 m s^{-1} updraft; (c),(d) maximum depth of 3 g kg^{-1} moisture perturbation; (e),(f) duration of 5 m s^{-1} updraft; and (g),(h) duration of 3 g kg^{-1} moisture perturbation, where all of the experiments (left) are averaged over all initial distances or (right) are averaged over the initial temperature deficits. Because there is no moisture present in the DRY group of simulations, the respective areas for these experimental suites are left blank in (c), (d), (g), and (h). Black dots are placed for the maximum values in each experiment suite, with multiple dots if there are duplicates of the maximum value. The thresholds of 5 m s^{-1} and 3 g kg^{-1} are chosen arbitrarily. Although the magnitudes of the depths/durations are sensitive to these thresholds, the trends of depth/duration with the tested parameters are not sensitive to these thresholds (not shown).

W_max peaks around an "optimal distance" of ~2.5 km and decreases for distances smaller or larger than this optimum. Peak W_max values at this ~2.5 km optimal distance is evident across the other experiment suites as well (Fig. 6b) regardless of the background environmental conditions. The updraft depths also seem to share this non-monotonicity (Fig. 7b); however, the trend of updraft duration with initial distance varies depending on the background environment (Fig. 7f). The optimal

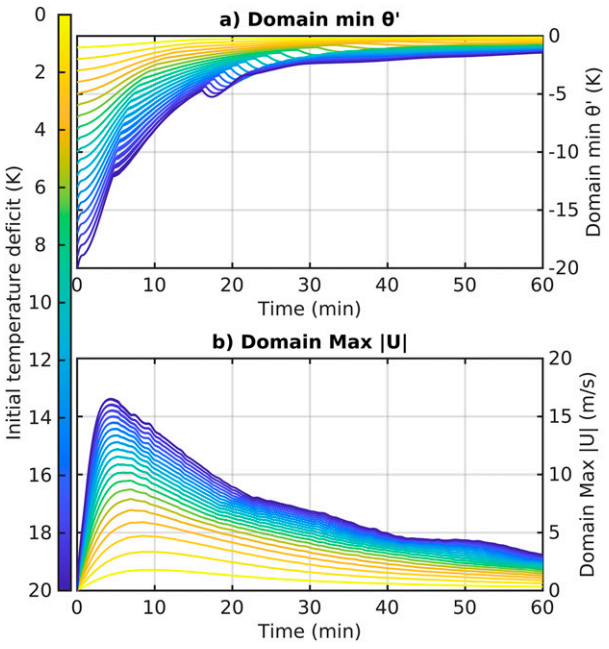

FIG. 8. The effect of the initial temperature deficit on cold pool dissipation and horizontal winds, showing time series of (a) domain minimum potential temperature perturbation and (b) domain maximum absolute value of horizontal for all simulations in the WK suite with an initial distance of 13.6 km. Darker colors in (a) and (b) indicate colder initial cold pool temperature deficits as shown by the color bar.

distance between colliding cold pools in producing the strongest updrafts, assuming all else equal, therefore appears to be robust and somewhat remarkably independent of background environments. While an optimal distance of 2.5 km appears relatively small, phenomena such as neighboring cells in a multicellular convective system can produce cold pools at such distances, as do precipitating boundary layer cumulus. This result may have important implications for the subsequent production of convection and/or convective organization.

The relationship between rvp_max and initial distance is also non-monotonic in the WK experiment suite (Fig. 5b). However, peak values of rvp_max occur for much greater and more variable initial distances than W_max (Figs. 5b, 6d, and 7d,h). Thus, unlike for mechanical forcing, there is no clear optimal initial distance that produces peak thermodynamic forcing.

Time series of the domain maximum vertical velocity for the 10 K simulations of the WK, DI, NT, and SK experiment suites are shown in Figs. 9a–d in the purple to yellow lines. The red and black lines are explained below. The peaks of these curves correspond with the cold pool collisions. It is clear from this figure that as the initial separation distance increases (indicated by lighter colored lines), the collisions occur later and later in time. This behavior is expected and was also seen in MH20's Fig. 7a. The optimal distance is also evident in this figure, as in each subplot, the highest peak is not for the most closely spaced cold pools (the darkest of purple lines) but rather for those starting out slightly farther apart (lighter purple lines). Enhancements in water vapor due to cold pool collisions decrease more slowly and, in some cases, non-monotonically with time than those for vertical velocity (Figs. 9e–h). Additionally, comparing the timing of these enhancements in the WK suite demonstrates that peaks in water vapor mixing ratio occur after those in vertical velocity for all of the experiments shown (Fig. 9i). This can be explained by the fact that the water vapor mixing ratio perturbations are generated by the collisional updrafts, and only decrease once that updraft has collapsed. This lag between an increase in vertical velocity and an increase in water vapor mixing ratio should occur regardless of what causes the increase in vertical velocity.

Cold pools that start closer together will be colder when colliding, so as the initial distance between cold pools decreases, W_max should increase. This is the case for all but the closest initial distances tested where this trend reverses. This reversal can be explained in terms of kinetic and potential energy. The domain-integrated kinetic energy from the 10 K initial temperature deficit simulations in the WK experiment suite is shown in Fig. 10a. The initial increase in kinetic energy with time is due to the fact that it takes time for the cold pools to generate kinetic energy from their initial potential energy, while the later decrease in kinetic energy is due to the dissipation of the cold pools. A balance between the generation of kinetic energy and dissipation of the cold pools explains the optimal distance. For cold pools that start closer together than the optimal distance of ~2.5 km, the cold pools do not have enough time to convert sufficient potential energy into kinetic energy before colliding, resulting in reduced convergence during the collision, and thus diminished W_max. For cold pools that start farther apart than the optimal distance, the cold pools have dissipated appreciably before colliding, thereby reducing kinetic energy and resulting in diminished W_max.

The different phases of density current evolution may also help to explain the optimal distance. Huppert and Simpson (1980) noted that density currents evolve through distinct phases after their initial acceleration: first, a slumping phase, where motion in the surrounding fluid slows the current; next, an inertial phase, where inertial forces balance the buoyant force; and finally, a viscous stage, where viscous forces balance the buoyant force. Cold pools that are too close together and collide during the initial acceleration or the slumping phase would have diminished W_max due to motions in the surrounding atmosphere slowing cold pool propagation. However, such motions would be insignificant to cold pools that collide during the inertial phase. Thus, a pair of cold pools spaced so that they collide early in the inertial phase, before they have slowed appreciably, would seemingly have the greatest W_max. This line of reasoning is speculative, and further analysis is needed to confirm this explanation of the optimal distance in terms of density current phases.

While the relationship between W_max and the initial distance shows a clear and robust optimal distance, the relationship between rvp_max and the initial distance does not. It is hypothesized that this is a result of the following process. The

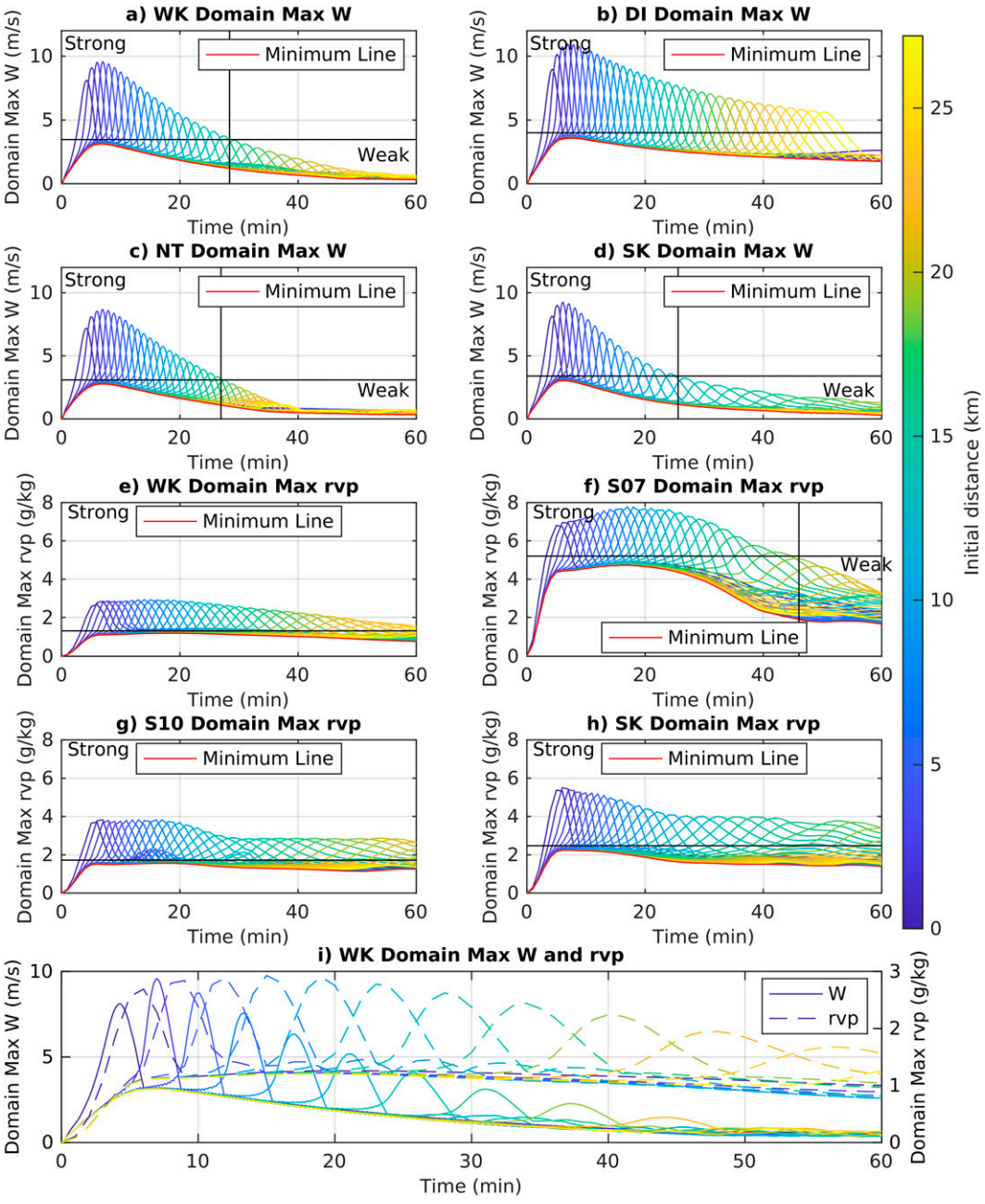

FIG. 9. Time series of domain maximum vertical velocity from the 10-K initial temperature deficit simulations from the (a) WK, (b) DI, (c) NT, and (d) SK experiment suites. Lighter colors indicate simulations with larger initial distances between cold pools. The red line is the smallest domain maximum vertical velocity at each time (see the text for additional description), and the horizontal black line is 1.1 times the peak of this red line. Simulations with peaks above this horizontal black line have mechanically strong collisions (as defined in section 4b). A vertical black line is placed to separate the last strong collision from the first weak collision. Those below and to the right of the black lines have weak collisions. All collisions in DI are strong. Also shown are time series of domain maximum water vapor mixing ratio perturbation from the 10-K initial temperature deficit simulations from the (e) WK, (f) S07, (g) S10, and (h) SK experiment suites. Thermodynamically strong collisions indicated in (e)–(h) are analogous to mechanically strong collisions in (a)–(d). (i) Domain maximum vertical velocity (solid lines) and water vapor mixing ratio perturbation (dashed lines) are overlaid for 10-K initial temperature deficit simulations and every third initial distance tested in the WK experiment suite.

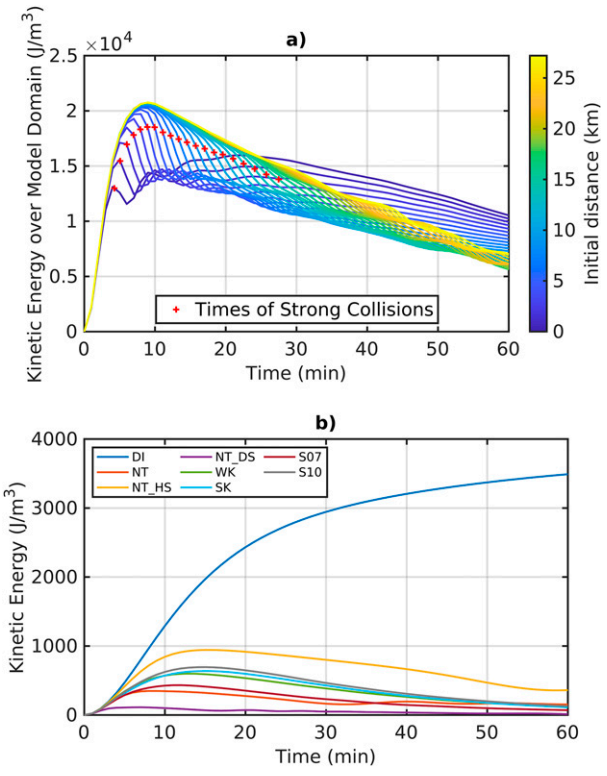

FIG. 10. Evolution of kinetic energy during cold pool collisions. (a) The time series of kinetic energy summed over the model domain from the 10-K initial temperature deficit simulations of the WK experiment suite. As in Fig. 9, lighter colors indicate simulations with larger initial distances between cold pools. For every simulation with a strong collision, a red cross is placed on that simulation's line, marking the time at which the cold pools collide. (b) Time series of kinetic energy summed over the model domain for all simulations with an initial 1-K temperature deficit and an initial distance of 13.6 km.

initial large vertical velocity at the cold pool heads lofts moist environmental air from low levels. This creates "moist zones" of enhanced water vapor mixing ratio around the heads of the cold pools. While the vertical velocity at the cold pool heads will decrease with time as the cold pools dissipate, these moist zones are advected horizontally with the cold pool heads and do not diminish nearly as rapidly over time. Thus, for large initial distances, colliding cold pools will generate relatively small mechanical forcing, but large thermodynamic forcing as their moist zones collide. A careful examination of Figs. 2b–d shows the vertical velocity at the cold pool head decreasing with time, while the moist zone at the cold pool head remains relatively steady. Comparing Figs. 9a–d with Figs. 9e–h also shows that the domain maximum water vapor mixing ratios decrease much more slowly in time than the domain maximum vertical velocities, further supporting this moist zone argument.

With the relationship between the W_max/rvp_max and the initial distance between cold pools now explained, Fig. 11 can be used to define "strong" and "weak" collisions. Figure 11a shows time series of domain maximum vertical velocity for all simulations in the WK suite with an initial temperature deficit of 10 K and is the same as Fig. 9a but with the black and red lines removed. For clarity and comparison, Fig. 11b plots only the time series of domain maximum vertical velocity for the WK_T10_D104 simulation. Note how there are two prominent peaks: a smaller "initial peak" around 7 min and a larger "collision peak" around 24 min. As these names imply, the initial peak is a peak in vertical velocity due to lifting in association with the initial, pre-collision spreading of the cold pools and occurs independently of other cold pools in the domain. The collision peak on the other hand is the peak in vertical velocity due to the collision between the cold pools. Returning to Fig. 11a it can be observed that, except for cold pools that start very close together, the initial peaks of all the simulations are nearly identical while the collision peaks vary in time and size. Figure 11c is identical to Fig. 11a except a red "minimum line" is plotted. This minimum line is the minimum value of all domain maximum vertical velocities indicated by the purple through yellow lines. Figure 11d is identical to Fig. 11b, as it only shows a time series from the WK_T10_D104 simulation, except the minimum line from Fig. 11c is included along with a horizontal black line. Note how the minimum line in Fig. 11d closely tracks with the domain maximum vertical velocity until the collision peak. The minimum line therefore represents the situation when the effects of cold pool collisions are removed. Thus, we are left with a line that includes the initial peak but not any collision peaks. The black horizontal line in Fig. 11d is plotted at 1.1 times the peak of the minimum line, for computational reasons, and represents the vertical velocity produced from the initial peak. As can be seen in Fig. 11d, the collision peak from the simulation plotted is greater than the initial peak (or equivalently the black horizontal line). Such collisions are defined as "mechanically strong." On the other hand, simulations where the initial peak is greater than the collision peak, such as the WK_T10_D176 simulation plotted in Fig. 11f, are defined as "mechanically weak." In mechanically weak collisions, the initial lofting arising from the spreading cold pool is larger than that induced by the cold pool collisions. Figure 11e is identical to Fig. 11c except with the black horizontal line showing the vertical velocity of initial peak and a black vertical line to separating the last mechanically strong collision from the first mechanically weak collision. Similar red and black lines are plotted in Figs. 9a–d to identify mechanically strong and weak collisions in other environments tested. Note that the DI environment in Fig. 9b has no mechanically weak collisions. "Thermodynamically strong" and "thermodynamically weak" collisions are similarly identified, except time series of domain maximum water vapor mixing ratio perturbation are used instead of time series of domain maximum vertical velocity (Figs. 9e–h).

This terminology of mechanically strong and weak collisions is therefore proposed as a simple binary metric to determine if a collision meaningfully increases W_max beyond the vertical velocity produced by the initial spreading of the cold pools. There may be strong collisions where the initial spreading of the cold pools produces insufficient lifting to initiate convection, but sufficient lifting occurs during the collision to initiate convection. For weak collisions, on the other hand, if

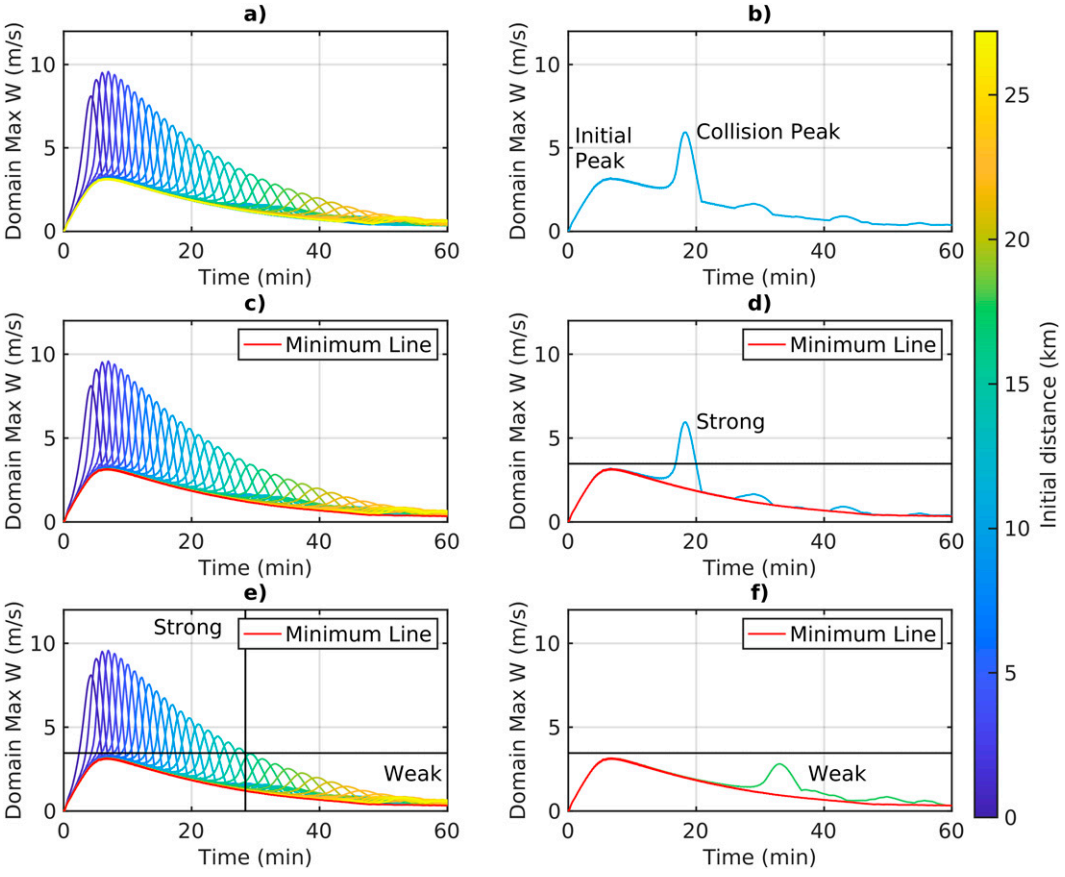

FIG. 11. Graphical description of "strong collisions" and "weak collisions." (a) Time series of domain maximum vertical velocity from the 10-K initial temperature deficit simulations from the WK suite. (c) As in (a), but with a red minimum line representing the smallest domain maximum vertical velocity at each time. (e) As in (c), but with a horizontal black line at 1.1 times the peak of the red minimum line to separate strong and weak collisions and a vertical black line separating the last strong collision from the first weak collision. (b) As in (a), but only plotting domain maximum vertical velocity for the simulation with an initial distance of 10.4 km. (d) As in (b), but including the red minimum line and black horizontal line at 1.1 times the peak of the red minimum line, thereby showing that the simulation presented is a strong collision. (f) As in (d), but showing a weak collision.

convection is to be initiated, it is most likely to occur with the initial spreading of the cold pools. Thus, using W_max as a proxy for mechanical forcing and ignoring thermodynamic forcing, mechanically strong collisions increase the chance of convection initiation beyond the lifting associated with the initial spreading of the cold pools, whereas mechanically weak collisions do not. By analogous logic, thermodynamically strong cold pool collisions increase rvp_max, and thus implicitly increase the chance of convection initiation, beyond that produced by the initial spreading of the cold pools.

The percentage of mechanically and thermodynamically strong collisions increases as the initial temperature deficit increases and the initial distance between cold pools decreases (Figs. 6e–h). Considering all of the simulations conducted here, 58.3% of collisions are mechanically strong. For the environments with moisture, thermodynamically strong collisions (74.4% of collisions) are more common than mechanically strong collisions (50.8% of collisions). Trends in strong/weak collisions for changes in the environment will be discussed in the following section.

c. *The effect of the environment*

Two specific environmental factors form the focus of the analysis of the environmental effects on cold pool collisions. The first is the low-level static stability, defined as the base state Brunt–Väisälä frequency between 25 and 975 m AGL. The second is the low-level differential moisture, defined here as the base state water vapor mixing ratio at 25 m AGL minus the base state water vapor mixing ratio at 975 m AGL. These levels are chosen as 25 m AGL is the lowest scalar model level while 975 m AGL is the highest scalar model level below 1000 m AGL, which is the top of the initial cold bubbles.

Comparing the DI, NT_HS, NT, and NT_DS experiment suites, where the low-level static stability steadily increases from 0 to 0.02 s^{-1}, it is clear that increasing the low-level static stability decreases the W_max produced by collisions and the

percentage of mechanically strong collisions (Figs. 6a,b,e,f). Additionally, updrafts are shallower and shorter-lived as static stability increases (Figs. 7a,b,e,f). This is due to both the stabilization effect, in which there is greater resistance to upward motion as low-level static stability is increased, and seemingly also the effect of gravity waves. Liu and Moncrieff (2000) argued that radiation of energy by gravity waves does not apply to cases in which low-level stable layers trap gravity waves within the layer. However, domain total kinetic energy in experiments with any static stability, whether limited to the surface (NT, NT_HS, and NT_DS), or in a continuously stratified atmosphere (WK, SK, S07, S10), is greatly reduced relative to the experiment using a dry isentropic environment (DI) (Fig. 10b). Thus, it appears that while gravity waves remain trapped near the surface in the nocturnal cases (NT, NT_HS, and NT_DS), they are still capable of radiating energy away from the cold pools and dissipating it as in the continuously stratified atmospheres. As the stabilization effect and the effect of gravity waves both occur in statically stable environments, it is unclear how to disentangle these two effects and compare their individual impacts on W_max.

The effect of even minimal low-level static stability on cold pool collisions can be large. The dry isentropic (DI) and half-stability nocturnal (NT_HS) experiment suites were rerun for 4 h to examine this effect. These suites were chosen as DI has no low-level static stability, while NT_HS has the lowest nonzero value of any of the environments tested, with low-level static stability of 0.005 s^{-1}. For large initial cold pool distances and the smallest initial temperature deficits, collisions may not occur within the 1-h time simulation duration. Rerunning NT_HS for four hours (Fig. 12b) demonstrates that even with minimal low-level static stability, collisions cease to be mechanically strong well before an hour of simulation time, as the cold pools with a 1-K initial temperature deficit dissipate quickly. However, this is not the case in DI suite, where all of the collisions are mechanically strong, even with the smallest initial temperature deficit (1 K) and farthest initial distance (27.2 km) tested (Fig. 12a). These results indicate that cold pool collisions should produce greater mechanical forcing in boundary layers that are increasingly well mixed and closer to neutral stability.

Last, comparing the WK, S10, SK, and S07 simulations, with low-level differential moisture of 3.2, 4.5, 6.5, and 7.2 g kg^{-1}, respectively, it is clear that as differential moisture increases, rvp_max increases (Figs. 6c,d). The depths and durations of these moisture perturbations also increase as differential moisture increases (Figs. 7c,d,g,h). This is due to the vertical advection of environmental water vapor [Eq. (5)]. For the same positive vertical velocity, a greater differential moisture will lead to a greater positive increase in water vapor mixing ratio perturbation with time.

d. Relative importance and summary of effects

The difference in mean W_max between all simulations with the maximum and minimum tested values of each parameter is shown in Fig. 13a. This indicates that mechanical forcing is most sensitive to the initial temperature deficit, followed by the low-level static stability, and last initial cold pool distance (Fig. 13a) for the suite of values tested here. Mechanical forcing increases nearly linearly as cold pools get colder (Fig. 13b), peaks at the optimal distance of ~2.5 km and decreases away from that distance (Fig. 13c), and non-monotonically decreases as the low-level static stability increases (Fig. 13d).

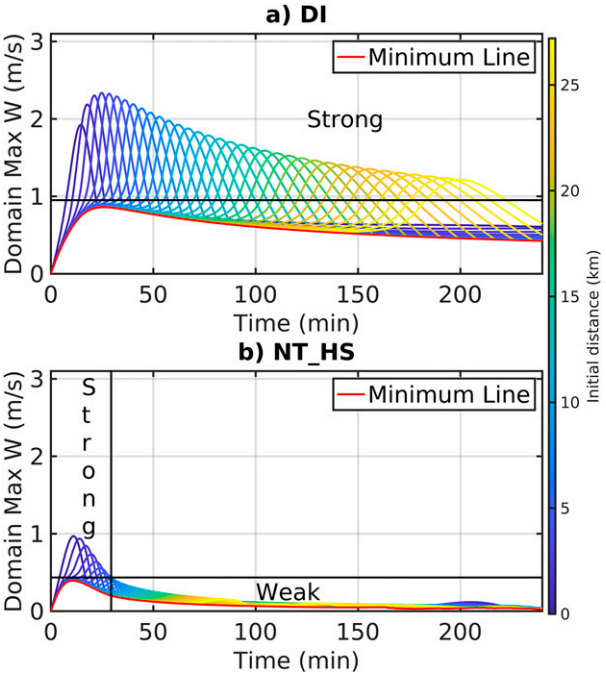

FIG. 12. Effect of static stability on vertical velocity from cold pool collisions: as in Figs. 9a–d, but for the 1-K initial temperature deficit simulations from the (a) DI and (b) NT_HS experiment suites after 4 h. Note that all of the collisions are strong (see section 4b for definition) in the DI environment, which has no static stability.

Similarly, the impact of each parameter on rvp_max is summarized in Fig. 14. Thermodynamic forcing is most sensitive to the initial temperature deficit, followed by the low-level differential moisture, and last the initial cold pool distance (Fig. 14a). Thermodynamic forcing greatly increases as cold pools get colder (Fig. 14b), slowly and non-monotonically decreases as initial distance increases (Fig. 14c), and greatly increases as low-level differential moisture strengthens (Fig. 14d). It is important to note that for both the updraft velocity and water vapor, the predominance of the tested parameters is the same.

5. Conclusions

Collisions between convective cold pools can enhance vertical velocity (mechanical forcing) and water vapor mixing ratio (thermodynamic forcing) (Droegemeier and Wilhelmson 1985b,a; Tompkins 2001; Torri et al. 2015), thereby initiating new, potentially severe convection (Droegemeier and Wilhelmson 1985b,a; Wilson and Schreiber 1986; Lima and Wilson 2008). While it is known that cold pool properties are sensitive to the background environment (e.g., Liu and

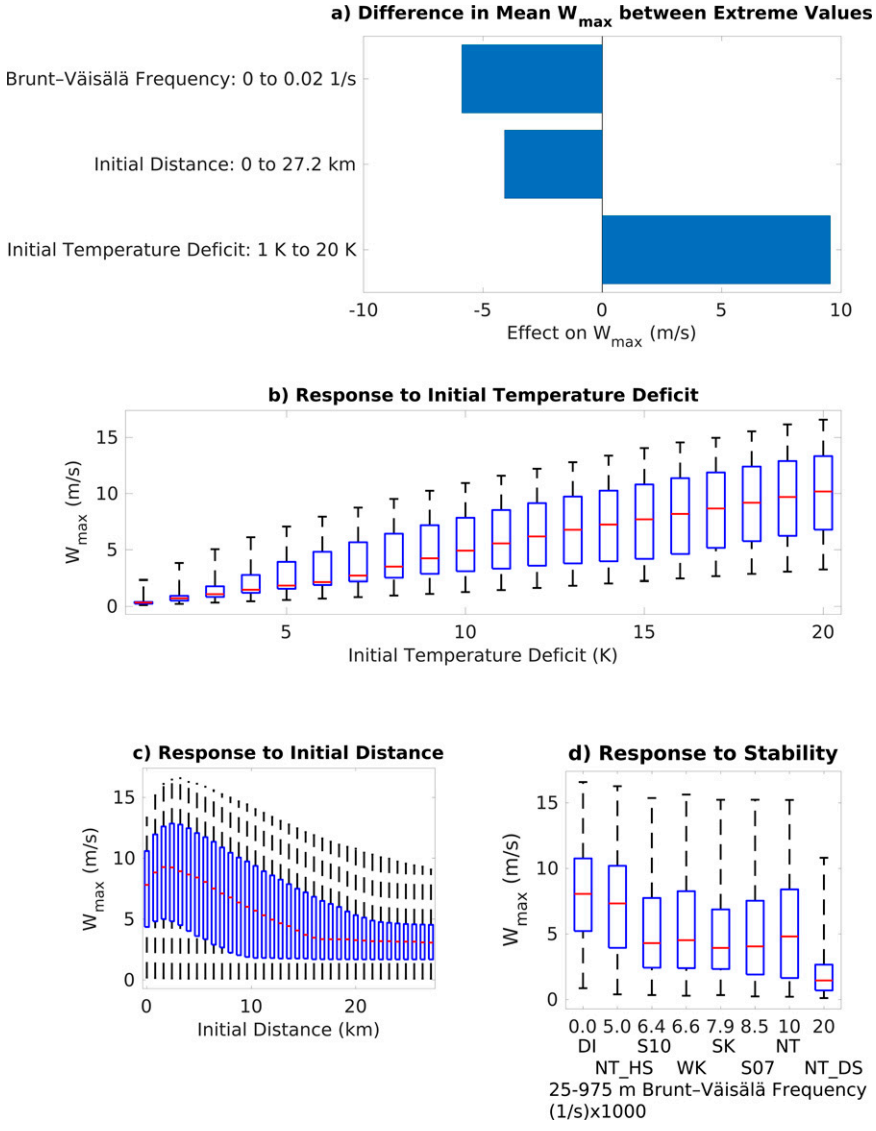

FIG. 13. Summary of the effects of each parameter tested on the vertical velocity generated as a result of the cold pool collisions: (a) Difference in mean W_max between all simulations with the maximum and minimum tested values of each parameter, and boxplots of W_max versus (b) initial temperature deficit, (c) initial distance, and (d) low-level static stability. Note that the abscissa in (d) is nonlinear for more clarity. Plot whiskers extend to extreme values.

Moncrieff 2000), the effects of the environment on cold pool collisions have not been thoroughly examined. The objective of this study has been to determine the sensitivity of mechanical and thermodynamic forcing from cold pool collisions to the environment.

A large number of idealized, 2D simulations were run in which 1) the initial cold pool temperature deficits, 2) the initial edge-to-edge distance between the colliding cold pools, and 3) the background environment in which the collisions are occurring were varied. While in reality the temperature deficit of a cold pool is dependent on its background environment, these parameters are tested independently here. The DRY group of simulations had no water vapor while the MOIST group of simulations had water vapor. Water vapor was not allowed to condense in any simulation in order to isolate the impact of cold pools from the possible subsequent impact of moist convection. The following conclusions have been drawn from this research:

- Mechanical and thermodynamic forcing from cold pool collisions are both most sensitive to the initial temperature deficit of the cold pools. Cold pools that start colder consistently produce stronger, deeper, and longer-lasting mechanical forcing and thermodynamic forcing than initially warmer cold pools. This is due to greater initial potential energy leading to greater horizontal winds and stronger

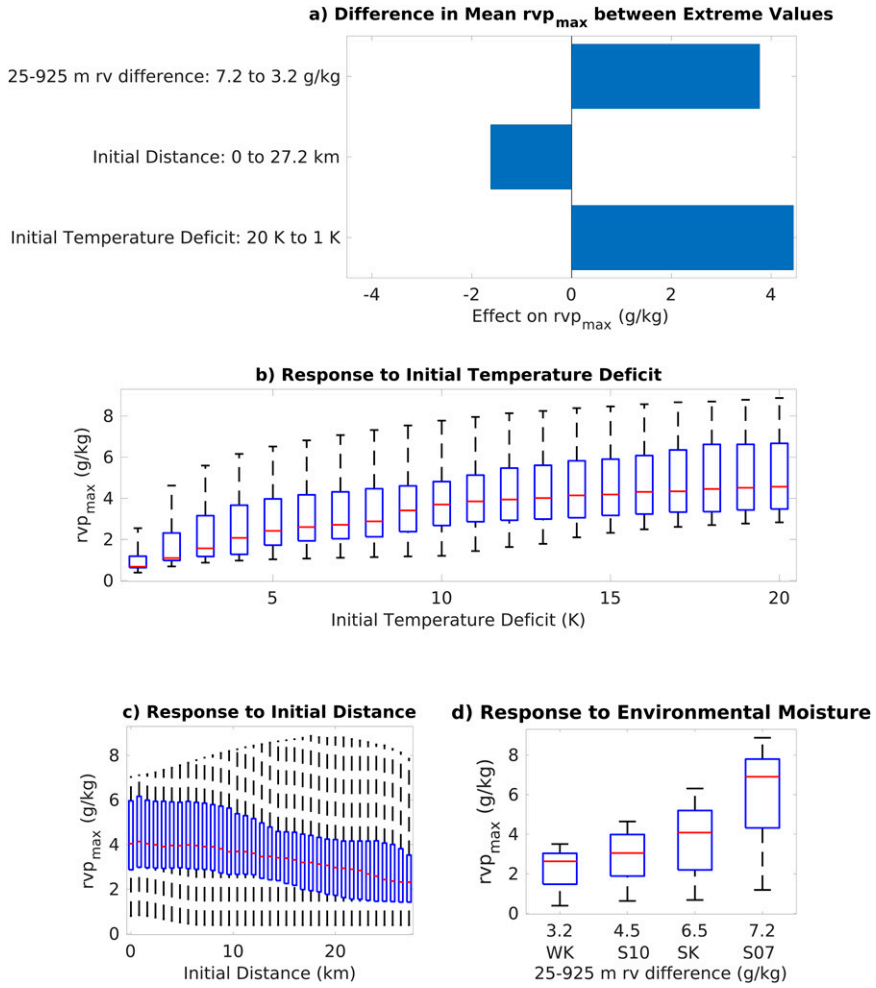

FIG. 14. As in Fig. 13, but for water vapor mixing ratio: (a) Difference in mean rvp_max between all simulations with the maximum and minimum tested values of each parameter, and boxplots of rvp_max versus (b) initial temperature deficit, (c) initial distance, and (d) low-level height differential moisture.

subsequent horizontal convergence during collisions. These collisions, in turn, generate a more intense updraft that vertically advects more moisture. As colder cold pools are more common in continental environments than in maritime environments, this suggests that cold pools collisions in continental environments produce greater mechanical and thermodynamic forcing.

- The second largest impact on mechanical and thermodynamic forcing is from the environment in which the cold pools existed. Increased low-level static stability decreases the magnitude, depth, and duration of vertical velocity generated from collisions through the stabilization effect and the radiation of energy away by gravity waves. Such findings are in keeping with prior work by Liu and Moncrieff (2000). Greater low-level differential (25–975 m AGL) moisture increases the moisture advected during collisions leading to greater thermodynamic forcing.
- The initial distance between the cold pools had the smallest impact on mechanical and thermodynamic forcing. Mechanical forcing robustly peaks around an *optimal initial distance* of ~2.5 km for all of the tests conducted here. Cold pools that start closer than the optimal distance do not have enough time to build horizontal wind velocity before colliding, while cold pools that start farther apart than the optimal distance dissipate too much before colliding, leading to decreased mechanical forcing in both cases. Cold pools colliding during their initial acceleration or the slumping phase (Huppert and Simpson 1980) is another possible explanation for the optimal distance. Thermodynamic forcing peaks at initial distances much larger than the ~2.5-km optimal distance for mechanical forcing. While mechanical forcing helps drive thermodynamic forcing by advecting moist air from near the surface to higher heights in the boundary layer, this result shows that there is not a one-to-one relationship between these forcings. It is hypothesized that this occurs as a result of the "moist zones" at the cold pool heads that do not diminish in time as rapidly as the vertical velocity at the cold pool heads. The optimal distance may be sensitive to parameters

not tested in this work, such as the initial size of the cold pools, although this would need to be assessed in a future study.

- A classification of cold pool collisions into categories of mechanically "strong" and "weak" and thermodynamically "strong" and "weak" was developed. In time series of maximum vertical velocity from cold pool collisions, an "initial peak" and later "collision peak" are evident. The former represents the vertical velocity produced from the initial outward spreading of the cold pools while the latter shows the vertical velocity produced from the actual collision of the cold pools. Collisions where the collision peak is greater than the initial peak are termed "mechanically strong" and collisions where the initial peak is greater than the collision peak are termed "mechanically weak." Thermodynamically strong/weak collisions are defined analogously by looking at time series of maximum water vapor mixing ratio perturbation. These categories are useful in that only strong collisions increase the likelihood of convection initiation beyond that associated with the lifting driven by the initial spreading of the cold pools.
- In environments with moisture, thermodynamically strong collisions (74.4% of collisions) occur more frequently than mechanically strong collisions (50.8% of collisions). For the range of idealized and observed, continental and maritime environments tested, this suggests thermodynamic forcing from cold pool collisions may initiate new convection more frequently than mechanical forcing from cold pool collisions.

The trends found in this study should be further explored and validated using 3D simulations given the potential shortfalls of 2D simulations in representing cold pool processes, such as the breakdown of Kelvin–Helmholtz waves. Furthermore, there remains a vast parameter space to explore regarding cold pool collisions including the initial height of the cold pools, the impact of surface fluxes, asymmetric collisions between cold pools, and the impact of wind shear (e.g., Rotunno et al. 1988). A similar study to this could be conducted in which the role of these parameters could be quantitatively assessed. Also, cold pools in dry isentropic environments were found to have much larger kinetic energy, vertical velocity, and numbers of mechanically strong collisions relative to environments with even minimal stable stratification. It is therefore suggested that future work focused on modeling cold pool collisions should not utilize dry isentropic environments alone without comparing the results with other more realistic environments.

Convective storms remain a major human and economic threat, and thus the ability to forecast processes that lead to their initiation is critical. This work has determined environmental conditions that can increase the probability of a cold pool collision initiating new convection. It has also suggested that cold pool collisions frequently increase thermodynamic forcing over and above the action of individual cold pools, but that individual cold pool lifting is about as prevalent as the lifting through cold pool collisions when mechanically initiating new convection. We hope these results can be used both to improve convective parameterizations in forecast and regional models and by forecasters trying to anticipate convective events in near real time.

Acknowledgments. This work was supported by NASA Grant 80NSSC18K0149 and NSF Grant AGS-2019947. We thank the three anonymous reviewers who provided insightful comments that benefited this work.

Data availability statement. Model source code available at a GitHub repository (https://github.com/nmfalkcsu/The-Role-of-Cold-Pool-Collisions-in-Convective-Initiation).

REFERENCES

Byers, H. R., and R. R. Braham, 1949: *The Thunderstorm: Report of the Thunderstorm Project*. U.S. Government Printing Office, 287 pp.

Chandra, A. S., P. Zuidema, S. Krueger, A. Kochanski, S. P. Szoeke, and J. Zhang, 2018: Moisture distributions in tropical cold pools from equatorial Indian Ocean observations and cloud-resolving simulations. *J. Geophys. Res. Atmos.*, **123**, 11 445–11 465, https://doi.org/10.1029/2018JD028634.

Craig Goff, R., 1976: Vertical structure of thunderstorm outflows. *Mon. Wea. Rev.*, **104**, 1429–1440, https://doi.org/10.1175/1520-0493(1976)104<1429:VSOTO>2.0.CO;2.

Drager, A. J., L. D. Grant, and S. C. van den Heever, 2020: Cold pool responses to changes in soil moisture. *J. Adv. Model. Earth Syst.*, **12**, e2019MS001922, https://doi.org/10.1029/2019MS001922.

Droegemeier, K. K., and R. B. Wilhelmson, 1985a: Three-dimensional numerical modeling of convection produced by interacting thunderstorm outflows. Part I: Control simulation and low-level moisture variations. *J. Atmos. Sci.*, **42**, 2381–2403, https://doi.org/10.1175/1520-0469(1985)042<2381:TDNMOC>2.0.CO;2.

——, and ——, 1985b: Three-dimensional numerical modeling of convection produced by interacting thunderstorm outflows. Part II: Variations in vertical wind shear. *J. Atmos. Sci.*, **42**, 2404–2414, https://doi.org/10.1175/1520-0469(1985)042<2404:TDNMOC>2.0.CO;2.

Engerer, N. A., D. J. Stensrud, and M. C. Coniglio, 2008: Surface characteristics of observed cold pools. *Mon. Wea. Rev.*, **136**, 4839–4849, https://doi.org/10.1175/2008MWR2528.1.

Feng, Z., S. Hagos, A. K. Rowe, C. D. Burleyson, M. N. Martini, and S. P. de Szoeke, 2015: Mechanisms of convective cloud organization by cold pools over tropical warm ocean during the AMIE/DYNAMO field campaign. *J. Adv. Model. Earth Syst.*, **7**, 357–381, https://doi.org/10.1002/2014MS000384.

Grant, L. D., and S. C. van den Heever, 2016: Cold pool dissipation. *J. Geophys. Res. Atmos.*, **121**, 1138–1155, https://doi.org/10.1002/2015JD023813.

Huppert, H. E., and J. E. Simpson, 1980: The slumping of gravity currents. *J. Fluid Mech.*, **99**, 785–799, https://doi.org/10.1017/S0022112080000894.

Intrieri, J. M., A. J. Bedard, and R. M. Hardesty, 1990: Details of colliding thunderstorm outflows as observed by Doppler lidar. *J. Atmos. Sci.*, **47**, 1081–1099, https://doi.org/10.1175/1520-0469(1990)047<1081:DOCTOA>2.0.CO;2.

Langhans, W., and D. M. Romps, 2015: The origin of water vapor rings in tropical oceanic cold pools. *Geophys. Res. Lett.*, **42**, 7825–7834, https://doi.org/10.1002/2015GL065623.

Lima, M. A., and J. W. Wilson, 2008: Convective storm initiation in a moist tropical environment. *Mon. Wea. Rev.*, **136**, 1847–1864, https://doi.org/10.1175/2007MWR2279.1.

Liu, C., and M. W. Moncrieff, 1996: A numerical study of the effects of ambient flow and shear on density currents. *Mon.*

Wea. Rev., **124**, 2282–2303, https://doi.org/10.1175/1520-0493(1996)124<2282:ANSOTE>2.0.CO;2.

——, and ——, 2000: Simulated density currents in idealized stratified environments. *Mon. Wea. Rev.*, **128**, 1420–1437, https://doi.org/10.1175/1520-0493(2000)128<1420:SDCIIS>2.0.CO;2.

Meyer, B., and J. O. Haerter, 2020: Mechanical forcing of convection by cold pools: Collisions and energy scaling. *J. Adv. Model. Earth Syst.*, **12**, e2020MS002281, https://doi.org/10.1029/2020MS002281.

Miller, S. D., A. P. Kuciauskas, M. Liu, Q. Ji, J. S. Reid, D. W. Breed, A. L. Walker, and A. A. Mandoos, 2008: Haboob dust storms of the southern Arabian Peninsula. *J. Geophys. Res.*, **113**, D01202, https://doi.org/10.1029/2007JD008550.

Purdom, J. F. W., 1976: Some uses of high-resolution GOES imagery in the mesoscale forecasting of convection and its behavior. *Mon. Wea. Rev.*, **104**, 1474–1483, https://doi.org/10.1175/1520-0493(1976)104<1474:SUOHRG>2.0.CO;2.

Rotunno, R., J. B. Klemp, and M. L. Weisman, 1988: A theory for strong, long-lived squall lines. *J. Atmos. Sci.*, **45**, 463–485, https://doi.org/10.1175/1520-0469(1988)045<0463:ATFSLL>2.0.CO;2.

Schlemmer, L., and C. Hohenegger, 2016: Modifications of the atmospheric moisture field as a result of cold-pool dynamics. *Quart. J. Roy. Meteor. Soc.*, **142**, 30–42, https://doi.org/10.1002/qj.2625.

Seigel, R. B., and S. C. van den Heever, 2012a: Dust lofting and ingestion by supercell storms. *J. Atmos. Sci.*, **69**, 1453–1473, https://doi.org/10.1175/JAS-D-11-0222.1.

——, and ——, 2012b: Simulated density currents beneath embedded stratified layers. *J. Atmos. Sci.*, **69**, 2192–2200, https://doi.org/10.1175/JAS-D-11-0255.1.

Sokolowsky, G. A., S. W. Freeman, and S. C. van den Heever, 2022: Sensitivities of maritime tropical trimodal convection to aerosols and boundary layer static stability. *J. Atmos. Sci.*, **79**, 2549–2570, https://doi.org/10.1175/JAS-D-21-0260.1.

Tompkins, A. M., 2001: Organization of tropical convection in low vertical wind shears: The role of cold pools. *J. Atmos. Sci.*, **58**, 1650–1672, https://doi.org/10.1175/1520-0469(2001)058<1650:OOTCIL>2.0.CO;2.

Torri, G., and Z. Kuang, 2016: Rain evaporation and moist patches in tropical boundary layers. *Geophys. Res. Lett.*, **43**, 9895–9902, https://doi.org/10.1002/2016GL070893.

——, and ——, 2019: On cold pool collisions in tropical boundary layers. *Geophys. Res. Lett.*, **46**, 399–407, https://doi.org/10.1029/2018GL080501.

——, ——, and Y. Tian, 2015: Mechanisms for convection triggering by cold pools. *Geophys. Res. Lett.*, **42**, 1943–1950, https://doi.org/10.1002/2015GL063227.

van den Heever, S. C., and Coauthors, 2021: The Colorado State University Convective CLoud Outflows and UpDrafts Experiment (C^3LOUD-Ex). *Bull. Amer. Meteor. Soc.*, **102**, E1283–E1305, https://doi.org/10.1175/BAMS-D-19-0013.1.

Weaver, J. F., and S. P. Nelson, 1982: Multiscale aspects of thunderstorm gust fronts and their effects on subsequent storm development. *Mon. Wea. Rev.*, **110**, 707–718, https://doi.org/10.1175/1520-0493(1982)110<0707:MAOTGF>2.0.CO;2.

Weisman, M. L., and J. B. Klemp, 1982: The dependence of numerically simulated convective storms on vertical wind shear and buoyancy. *Mon. Wea. Rev.*, **110**, 504–520, https://doi.org/10.1175/1520-0493(1982)110<0504:TDONSC>2.0.CO;2.

Wilhelmson, R. B., and C.-S. Chen, 1982: A simulation of the development of successive cells along a cold outflow boundary. *J. Atmos. Sci.*, **39**, 1466–1483, https://doi.org/10.1175/1520-0469(1982)039<1466:ASOTDO>2.0.CO;2.

Wilson, J. W., and W. E. Schreiber, 1986: Initiation of convective storms at radar-observed boundary-layer convergence lines. *Mon. Wea. Rev.*, **114**, 2516–2536, https://doi.org/10.1175/1520-0493(1986)114<2516:IOCSAR>2.0.CO;2.